

Starting points for the study of non-Fermi liquid-like properties of FeCrAs

BY

PATRICK JAMES O'BRIEN

BS, LeMoyne College, 2007

DISSERTATION

Submitted in partial fulfillment of the requirements for
the degree of Doctor of Philosophy in Physics
in the Graduate School of
Binghamton University
State of New York
2017

© Copyright by Patrick James O'Brien 2017
All Rights Reserved

Accepted in partial fulfillment of the requirements for
the degree of Doctor of Philosophy in Physics
in the Graduate School of
Binghamton University
State University of New York
2017

July 7, 2017

Charles Nelson, Chair
Department of Physics, Binghamton University

Michael Lawler, Faculty Advisor
Department of Physics, Binghamton University

Alexey Kolmogorov, Member
Department of Physics, Binghamton University

Pegor Aynajian, Member
Department of Physics, Binghamton University

Christof Grewer, Outside Examiner
Department of Chemistry, Binghamton University

Abstract

FeCrAs exhibits non-Fermi liquid-like behavior because of its odd combination of thermodynamic, transport, and magnetic properties. In particular, the resistivity of FeCrAs is not characteristic of a metal or an insulator and so remains a mystery. In this thesis, we seek a model to describe its properties. In FeCrAs, local moments reside on the Cr sites, and there is some conduction. We study the simplest possible model on the kagome lattice that features local moments and itinerant electrons, the kagome Kondo Lattice Model. We present the phase diagram of this model, which features a host of complex spin orders, one of which is the $\sqrt{3} \times \sqrt{3}$, the experimentally observed magnetic ground state in FeCrAs. The kagome Kondo Lattice Model, having one itinerant d-orbital band on the kagome lattice, does not fully capture the microscopic physics of FeCrAs. The kagome Kondo Lattice Model also will not describe the mutilation of the Fermi surface. To investigate the microscopic properties, we calculated LDA and LDA+U results. These results and GGA results from another group all exhibit high d-orbital density of states at the Fermi energy as well as low p-orbital density of states at the Fermi energy. The DFT results motivated us to construct a model based on the chemistry and full geometry of the FeCrAs crystal. The model we construct is an effective hopping model consisting of only d-orbital operators that we call the Optimal Overlap Hopping Model (OOHM). We calculate the band structure that results from the OOHM, and this band structure can be compared to ARPES measurements. As an example of how one can use the OOHM, we

calculate a dynamic spin structure factor from within the OOHM, and we compare it to neutron scattering data. We consider both the OOHM and the Kondo Lattice Model on the kagome lattice as starting points from which we can launch studies of FeCrAs, and we present the existing theories for FeCrAs on a metallicity spectrum to illustrate the various perspectives from which FeCrAs is studied.

For my Parents, James and Therese

Acknowledgements

I would like to thank several people for their help during my education.

First, I thank my advisor from LeMoyne College, David Craig, for introducing me to some very important and beautiful ideas of physics. It is because of his love for physics and his phenomenal energy in the classroom that I chose to pursue physics further. I also thank Stamatios Kyrkos from LeMoyne College for allowing me to do research with him. This experience gave me an idea of what research would be like in graduate school.

I thank my current advisor, Michael Lawler, for introducing me to the vast field of physics that is condensed matter theory. He has taught me the true joy of discovering things on my own. We have calculated all of our results with code that I have written under his advisement (with the exception of diagonalizing matrices), and although debugging is a time of uncertainty and frustration, I am left with a sense of satisfaction knowing that, to some degree, I wrote all of the code myself.

Thank you to Alexey Kolmogorov and Pegor Aynajian for their valuable feedback. Their written criticism of earlier versions of the thesis were instrumental in preparing the thesis for publication.

Thank you to Shivam Ghosh for your collaborative effort of my material in chapter 2. I always liked an excuse to come visit you at Cornell. Those days were some of the most humbling and interesting days I experienced in graduate school.

Thanks to Turan Birol for calculating DFT results for FeCrAs. You were always

very helpful and friendly. Good luck in your endeavors!

Anthony Frachioni gave me some pivotal programming advice early on. He taught me about the stack limit in C++, and he encouraged me to allocate memory on the heap so that I didn't run into such limits. He also gave me some pointers on using Mathematica more efficiently. Thanks buddy.

Todd Rutkowski and I have had many useful discussions about our projects. He taught me about the essentials of writing a self-consistent mean field theory code, and I used this knowledge to write such a code in my project. Many thanks.

Jeremiah Dederick and I had many discussions about our projects. We often drew similarities between our projects, and we gave each other ideas about how to make progress. Jeremiah was also very helpful when I had questions about LaTeX; he is like a LaTeX encyclopedia. Thanks a bunch, bud.

Thanks to Danny Zlobinsky for his programming suggestions. Thanks to Dima Vartanian for helping me fix my dynamic spin structure factor code and for other programming advice. I hope to see you gentlemen soon.

Thank you to all of my friends for your support - Calford, Austin, Steve, Will, Kyle, Greg, Felix, Francis M., Andy, Erik, Imran, Samad, DC, Francis O., and anyone else I have omitted or forgotten, including newcomers to Binghamton. Your presence has made my time at Binghamton enjoyable.

Thank you to my future wife, Pam Caguana, for your support every day, your interest in what I do, and your jokes. Mostly the jokes, though.

Finally, thank you to my family for your support and for constantly reminding me what is important. I could not have done this without the help of both of my parents, Therese and James, during the toughest times. Thank you, as well, to my sister and brother, Colleen and Daniel, for all of the rage-inducing games of Yoshi we played on holiday. They really helped me unwind.

Contents

1 Understanding the metallicity spectrum with approaches to the study of FeCrAs	1
1.1 FeCrAs exhibits non-Fermi liquid-like behavior discovered in 2009	1
1.2 Previous approaches to studying FeCrAs: The insulating perspectives	5
1.3 Our approaches to the study of FeCrAs and the metallicity spectrum	8
2 A toy model : The Kondo Lattice Model on the kagome lattice	12
2.1 Motivation and History - Kondo Lattice Model	12
2.2 A simple motivation for the Kondo Lattice Model on the kagome lattice	15
2.3 Phase diagram of the Kondo Lattice Model on the kagome lattice	20
3 Optimal Overlap Hopping Model	28
3.1 DFT Results for FeCrAs	29
3.2 Constructing the Optimal Overlap Hopping Model(OOHM)	32
3.2.1 General form of the OOHM	32
3.2.2 Explicit form of the OOHM	33
3.2.3 Derivation of the OOHM	35
4 Beyond the Optimal Overlap Hopping Model	48
4.1 Onsite Mean Field Theory	48
4.1.1 Ferromagnetic Case	49
4.1.2 Q=0 case	51
4.2 Neutron Scattering and Dynamic Spin Structure Factor	52
4.3 Computational Cost	54
5 Conclusion	56
5.1 Summary of results	56
5.2 Discussion	57
A Hamiltonian and band structure of nearest neighbor kagome lattice : review	59
A.1 Writing a Hamiltonian	59
A.2 Calculating a band structure	61
B Silicon hybrid hopping model	65

List of Figures

- | | | |
|-----|--|---|
| 1.1 | Crystal structure of FeCrAs [1], figure taken with permission from from Wu et. al. [1]. Blue spheres denote Cr sites, green spheres denote Fe sites, and red spheres denote As sites. a) Tilted side view of the unit cell. The tetrahedron of As atoms that surrounds each Fe atom is shown as the shaded red area. Cr atoms lie on a distorted kagome lattice, denoted by the blue shaded area. Fe atoms lie near to one another in a grouping called a trimer. The Fe trimer is the shaded green region. b) Top view of the unit cell. Again we see the shaded areas denoting the tetrahedron of As atoms, the distorted kagome lattice of Cr atoms, and the trimer of Fe atoms. c) 3 unit cell \times 3 unit cell block of FeCrAs. | 2 |
| 1.2 | Resistivity measurement of FeCrAs [1], figure taken with permission from Wu et. al. [1]. Resistivity increases as temperature is decreased along the a direction. Along the c direction, resistivity decreases as temperature is lowered until 125K. At 125K, FeCrAs reportedly orders [1] into an antiferromagnetic $\sqrt{3} \times \sqrt{3}$ coplanar state. | 4 |
| 1.3 | Heat capacity of FeCrAs, figure taken with permission from Wu et. al. [1]. Where the plot intercepts the C/T axis is the Sommerfeld coefficient, which here is roughly 31 mJ/mol K ² . The effective mass associated with the Sommerfeld coefficient of FeCrAs is significantly lower than is seen in the heavy Fermion materials, but it is very large for a d electron material [1]. | 5 |
| 1.4 | Magnetic susceptibility of FeCrAs, figure taken with permission from [1]. The local maximum around $T_N = 125\text{K}$ signals the antiferromagnetic transition as the temperature is lowered. The system orders into a $\sqrt{3} \times \sqrt{3}$ state below T_N . The Wilson ratio given by the susceptibility is between 4 and 5 [1]. | 6 |

1.5 Spectrum of metallicity for the theories of FeCrAs. FeCrAs has a resistivity that is not metallic-like or insulating-like but something between these two extremes. Therefore, on the spectrum of metallicity, an appropriate description of the resistivity of FeCrAs would reside somewhere in the center. The antiferromagnetic Heisenberg model from Redpath et. al. [2] contains no electrons, so it is a completely insulating model which shows up on the left side of the spectrum. The Kondo Lattice Model on the kagome lattice contains electrons that couple with classical local spin moments, which means that it is a step in the metallic direction away from the antiferromagnetic Heisenberg model of Redpath et. al. [2]. The proposal of Rau and Kee [3] is also a step in the metallic direction from the insulating side. Rau and Kee's proposal features local Cr moments with the metallic hopping terms. On the metallic side of the spectrum resides the Optimal Overlap Hopping Model. We can add terms to the Optimal Overlap Hopping Model to move the model toward the insulating end of the spectrum, as we do in chapter 4. The Optimal Overlap Hopping Model with interactions added resides in the same part of the spectrum, because with interactions, we can move toward the insulating end of the spectrum.

10

2.1 The Cr sites are pyramidal coordinated by As sites in FeCrAs. We calculate non-ideal pyramidal crystal field splitting levels of the d electrons on the Cr sites. The degeneracies of the energy levels and the associated states are shown on the right. The most important result of this calculation is that the $3z^2 - r^2$ is the highest energy state. This fact becomes useful when considering the hopping model that results from placing these $3z^2 - r^2$ orbitals on the kagome lattice. This hopping model has only one hopping parameter because all pairs of these azimuthally symmetric $3z^2 - r^2$ orbitals are equally spaced, so their overlap integrals are all the same.

17

2.2 After calculating crystal field splitting diagrams, we fill the energy levels with the electrons available for Cr and Fe. Since we have assumed a Cr 2+ oxidation state, we have 6 electrons to place in the Cr splitting diagram. We fill the diagram assuming the high spin case, which assumes that the energy level spacings are smaller than the intraorbital Coulomb repulsion.

18

- 2.3 To create a toy model, we observe that the high spin case for the crystal field splitting calculated has a single electron in the highest energy level. We make a crude approximation that this electron in the highest energy level is an itinerant electron and that the bottom four electrons form a classical moment. We are motivated to call these bottom 4 electrons a classical moment because experiment has shown that the magnetic moment on the Cr sites be anywhere from 0.6 to 2.2 μ_B , and the classical moment that we have here is 2.0 μ_B . We then allow the itinerant electron to couple with the classical moment. This interaction along with a hopping term is the KLM.

2.4 Calculated exchange couplings in the RKKY limit. The first four couplings are plotted as a function of filling fraction in units of $\frac{J_k^2}{t}$. The plotted points result from second-order perturbation, as detailed in the text. J_1 is the nearest neighbor exchange coupling, J_2 is the next-nearest neighbor exchange coupling, and J_3 and J_{3h} are two types of next-next-nearest exchange coupling, with J_{3h} being the coupling associated with pairs of sites on opposite sides of a hexagon. The curves are the result of a fitting procedure explained in chapter 5 of Shivam Ghosh's PhD thesis. Figure from [4]

2.5 We find the ground state for the KLM of a given Kondo exchange coupling and filling fraction. We use the exchange tensor, which is calculated in the RKKY limit, to calculate the change in energy for each iteration of the Monte Carlo algorithm. This change in energy is used to define a Boltzmann factor used in the decision criterion of each Monte Carlo iteration (see simulated annealing procedure in text). The plot here is a common-origin plot of the ground state spin configuration resulting from simulated annealing for the 9 unit cell \times 9 unit cell system size at filling fraction $n = .5$

2.6 Variational phase diagram for the KLM in the (n, J_K) plane, with the filling range $n = (0, 1)$ and the Kondo coupling range $J_K = [0, 8]$. The points calculated along the J_K direction have spacings of 0.05t. The colored strip at the bottom is the RKKY phase diagram as a function of n , with the same color convention as the phases above. From [5].

3.1 The DFT results were obtained with VASP, version 5.2. The energy cutoff for the plane waves was 500 eV. The program uses the projector augmented plane wave method [6]. We used a Monkhorst-pack grid of 1 k-point per 0.3 \AA^{-1} in the reciprocal space. In addition to these settings, we also used $U = 4 \text{ eV}$ and 6 eV and $J = 0.7 \text{ eV}$ and 1.1 eV to obtain the four plots shown in Fig. 3.10. The plots here have been arranged with increasing J to the right and increasing U upward. We see that the plots are sensitive to changes in U , while the plots are not as sensitive to J . The band structures are plotted along the $\Gamma\text{-M}\text{-K}\text{-}\Gamma\text{-A}\text{-L}\text{-H}\text{-A}$ path.

3.2	The LDA and the GGA calculations. As a first attempt to compare the DFT results, we can compare the Γ point degeneracies with the hope of identifying similarities in the bands.	30
3.3	Band character for band structure calculated in the LDA. The As bands have very low density at the Fermi energy, while the Cr and Fe bands are dense at the Fermi energy. We use the band character information to justify writing an effective hopping model with only d-electron operators. The band character calculation for the LDA band structure shown here was done by Turan Birol [7].	31
3.4	Bond types that link a Cr to a neighboring Cr. Blue dots represent Cr atoms, while red dots represent As atoms. There are 4 distinct types of hopping connecting a Cr site to a neighboring Cr site. The wireframe shown is the parallelogram unit cell.	34
3.5	Bond types that link a Fe to a neighboring Fe. Green dots represent Fe atoms, while red dots represent As atoms. There are 3 distinct types of hopping connecting a Fe site to a neighboring Fe site.	35
3.6	Bond types that link a Cr to a neighboring Fe. Green dots represent Fe atoms, blue dots represent Cr atoms, and red dots represent As atoms. There are 2 distinct types of hopping connecting a Cr site to a neighboring Fe site.	36
3.7	Here is a top view of the FeCrAs crystal, taken from Wu et. al. [1]. Cr atoms are shown in blue, Fe atoms are shown in green, and As atoms are shown in red. The blue sites form a distorted kagome lattice.	37
3.8	We are writing a model with p-orbitals on As sites sigma-bonded to d-orbitals on neighboring Cr and Fe sites, therefore we direct the p-orbitals toward neighboring sites by taking a dot product of the vector that points from a d-electron site to a neighboring As site with the vector of p-orbitals, $\{p_x, p_y, p_z\}$, on said As site. Calculating this dot product for all As neighbors of a Cr gives the directed p-orbitals shown here.	38
3.9	Example of an optimal overlap orbital that results from running Monte Carlo. It is a linear combination of d-orbitals that optimizes the overlap with a directed p-orbital on a neighboring As site. There are 5 such orbitals on the Cr sites, as it is surrounded by a pyramid of As atoms.	41
3.10	p-orbitals on an As atom that is the nearest neighbor to two Cr atoms. We use these figures to construct the cluster model, Eq. (3.14).	42
3.11	Plot of Cluster Model and Effective Model eigenvalues vs bond angle (θ). We show that for the right choice of parameters, the effective model fits the cluster model. This gives us some justification for the $\cos(\theta)$ factor that enters the effective hopping term.	44
3.12	Band Structure of Optimal Overlap Hopping Model. We choose all hopping parameters to be 1 eV except for $t_{A,Cr}$, which we set to 6 eV. We choose these parameters to attempt to fit features of the LDA calculation. The band structure is plotted along the Γ -M-K- Γ -A-L-H-A path.	47

4.1	Results from the self-consistent mean field theory calculation, using the ferromagnetic case of the Hamiltonian in Eq. (4.10). Spin mean fields are shown for Cr(Blue) and Fe(Green) vs. iteration. It is interesting that Cr converges to a very small spin moment, while Fe stays quite large. Perhaps we can ascribe the dominance of the Fe spin mean field to the fact that we have chosen a ferromagnetic state, and Fe often tends to be ferromagnetic.	51
4.2	Momentum-averaged dynamic spin structure factor, $S(\omega)$, plotted between 0 meV and 6 meV. The independent axis here is the wavenumber in the calculation. For this calculation we calculated the structure factor along the b_1 direction in k space and summed over all k points. The benefit of making such a plot is that we observe that our model features spin excitations down to low energies.	54
4.3	Momentum-averaged dynamic spin structure factor, $S(\omega)$, plotted between 40 meV and 100 meV. The independent axis here is the wavenumber in the calculation. For this calculation we calculated the structure factor along the b_1 direction in k space and summed over all k points.	55
A.1	The kagome lattice is a triangular lattice with a basis. Along with lattices such as the triangular lattice and the pyrochlore lattice, it has been one of the central foci of the field of frustrated magnetism. The primitive vectors are $\vec{a}_1 = a\{1, 0\}$ and $\vec{a}_2 = a\{-\frac{1}{2}, \frac{\sqrt{3}}{2}\}$. The basis vectors are $\frac{1}{2}\vec{a}_1$, $\frac{1}{2}\vec{a}_2$, and $\frac{1}{2}(\vec{a}_1 + \vec{a}_2)$	60
A.2	Pictorial description of the density of states of various basic states of matter [8]	61
A.3	Brillouin zone of a hexagonal crystal structure with a path in red that is conventionally taken when plotting band structures for hexagonal structures [9]	62
A.4	Band structure of the nearest neighbor hopping model on the kagome lattice. The high-symmetry path taken is $\Gamma - M - X - \Gamma$. The flat band is a signal of the geometric frustration of the kagome lattice. The hopping parameter, t , is set to 1 in this calculation.	64
B.1	Diamond lattice of silicon. In the diamond lattice, each site is surrounded by a tetrahedron of neighboring sites [10].	66
B.2	One of silicon's hybrid orbitals. This is a linear combination of s and p orbitals that results in an orbital that points toward a vertex of a tetrahedron. These orbitals are the 4 (famous) sp^3 hybrid orbitals.	67
B.3	Brillouin zone of diamond [9]	70
B.4	Band structure of the model $H_{silicon}$ [11]. This band structure results from writing a nearest neighbor hopping model for silicon in the basis of the hybrid orbitals.	71
B.5	Band structure for silicon calculated by pseudopotential method, figure taken with permission from [12]. Looking at this band structure plot, we see that this is an indirect bandgap semiconductor.	71

B.6 Band structure for silicon in the hybrid orbital hopping model with sub-dominant hopping terms. Adding in these sub-dominant hopping terms introduces an indirect bandgap, making the band structure found with this model qualitatively like that of the real band structure of silicon. 72

Chapter 1

Understanding the metalicity spectrum with approaches to the study of FeCrAs

1.1 FeCrAs exhibits non-Fermi liquid-like behavior discovered in 2009

Non-Fermi liquid physics has garnered great interest in recent years. Non-Fermi liquids are materials that are not described by Landau's theory of Fermi-liquids. There are multiple paths to destroying or mutilating the Fermi surface, and there are many materials that have been found that exhibit non-Fermi liquid-like properties [13].

One non-Fermi liquid material that we are interested in is FeCrAs. FeCrAs, a stoichiometric mix of the elements iron, chromium, and arsenic, intrigues scientists as a result of the unusual properties it exhibits [1, 14–16]. It currently eludes classification, and it has attracted the interest of theorists and computationalists in recent years [2, 3, 17–20].

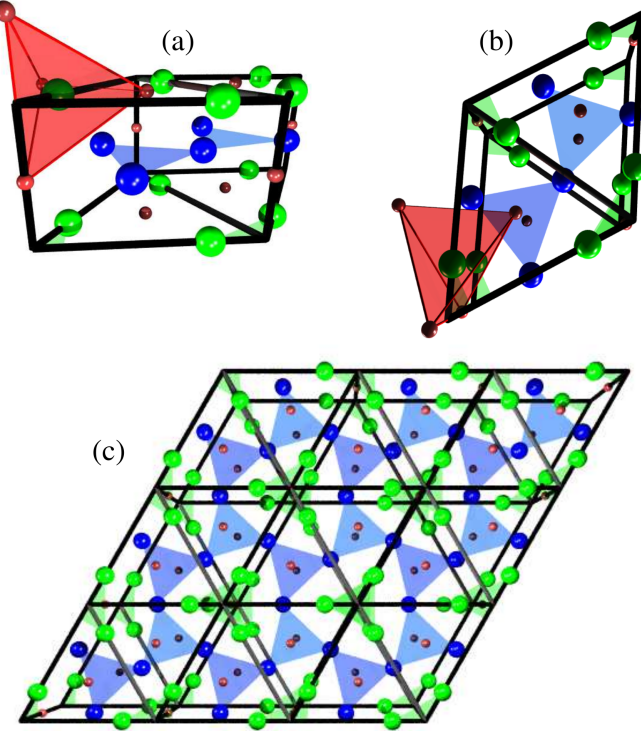


Figure 1.1: Crystal structure of FeCrAs [1], figure taken with permission from from Wu et. al. [1]. Blue spheres denote Cr sites, green spheres denote Fe sites, and red spheres denote As sites. a) Tilted side view of the unit cell. The tetrahedron of As atoms that surrounds each Fe atom is shown as the shaded red area. Cr atoms lie on a distorted kagome lattice, denoted by the blue shaded area. Fe atoms lie near to one another in a grouping called a trimer. The Fe trimer is the shaded green region. b) Top view of the unit cell. Again we see the shaded areas denoting the tetrahedron of As atoms, the distorted kagome lattice of Cr atoms, and the trimer of Fe atoms. c) 3 unit cell \times 3 unit cell block of FeCrAs.

Wu et. al. [1] at the University of Toronto grew single crystals of FeCrAs by melting stoichiometric quantities of high-purity Fe, Cr, and As. They grew several batches of crystals and then annealed the batches in a vacuum at 900° for 5 to 10 days. Some of the batches were characterized by X-ray powder diffraction, which showed that the samples crystallized in the $P\bar{6}2m$ structure, shown in Fig. 1.1.

There are 4 types of Wyckoff sites in the FeCrAs crystal [15], shown in Table 1.1. Additionally, the Pearson symbol is hP9. In FeCrAs, the As atoms form polyhedra around the Fe and Cr atoms which are of interest to us. When a first element in a

Element	Type of Wyckoff site	x	y	z
Cr	3g	0.564(4)	0	1/2
Fe	3f	0.240(2)	0	0
As	2c	1/3	2/3	0
As	1b	0	0	1/2

Table 1.1: Wyckoff positions of FeCrAs. There are 2 types of As sites, while there is one type of Fe site and one type of Cr site.

crystal is surrounded by a certain polyhedron of a second element, the first element is said to be coordinated by the second element. In FeCrAs, Fe is tetrahedrally coordinated by As, and Cr is pyramidal coordinated by As. These features will be important when we consider crystal field splitting in chapters 2 and 3.

After growing these samples, Wu et. al. [1] then measured the resistivity, heat capacity, and magnetic susceptibility. Their samples had varying quality, and the samples they reported were those that had the highest Néel temperature [1], the signal of which is observed in the magnetic susceptibility data.

The behavior of the resistivity of FeCrAs [1] is intriguing. As seen in Fig. 1.2, the resistivity rises as temperature is lowered. The resistivity is not metallic-like. In a metal, the resistivity decreases as temperature is lowered, because phononic contributions vanish as temperature goes to 0, and the electron-electron interactions go as T^2 . The values of resistivity reached for FeCrAs, though, are quite small. An insulator generally has a resistivity that increases exponentially with decreasing temperature, and the values of resistivity are large, signifying an insulating gap. Insulating-like behavior is not observed either. FeCrAs is neither an insulator nor a metal, and thus we seek a theory of a material that is somewhere between these two extremes.

The heat capacity of FeCrAs, on the other hand, is more ordinary. Its heat capacity is like that of a metal and thus can be described using Landau's Fermi liquid theory. In Fig. 1.3, we see that C/T vs. T^2 is linear, which is typical of a Fermi liquid. The plot of C/T vs T^2 , shown in Fig. 1.3, is linear, and it intercepts the

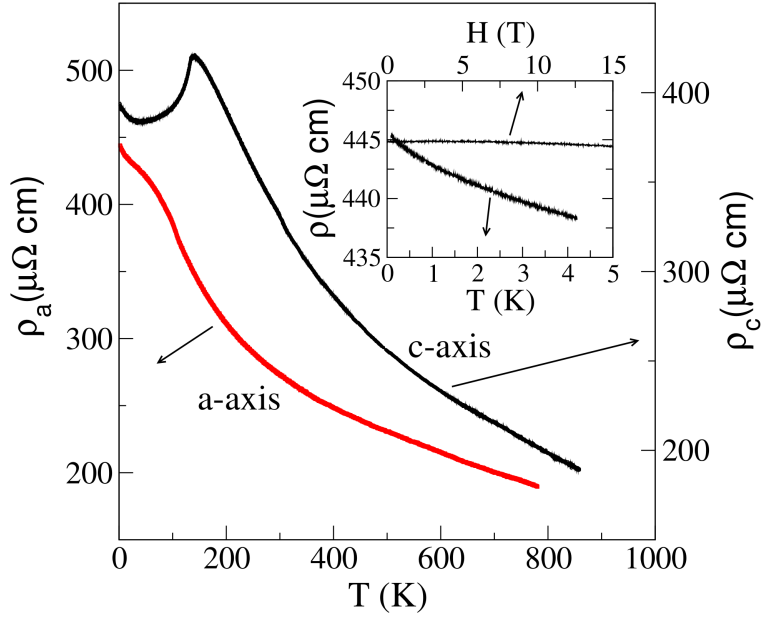


Figure 1.2: Resistivity measurement of FeCrAs [1], figure taken with permission from Wu et. al. [1]. Resistivity increases as temperature is decreased along the a direction. Along the c direction, resistivity decreases as temperature is lowered until 125K. At 125K, FeCrAs reportedly orders [1] into an antiferromagnetic $\sqrt{3} \times \sqrt{3}$ coplanar state.

C/T axis at roughly 31 mJ/mol K². The intercept of the C/T axis, which is the coefficient of the linear in T term of the heat capacity, is the Sommerfeld coefficient. The value of the Sommerfeld coefficient in FeCrAs is much smaller than that of the heavy fermion compounds, yet it is very large for a d-electron compound.

The resistivity and heat capacity of FeCrAs alone motivate further study. That the heat capacity can be described by Fermi liquid theory and the resistivity cannot has posed a problem that is unsolved to date.

In his thesis [16], D.G. Rancourt initiated the study of the magnetic structure of FeCrAs by presenting Mössbauer spectroscopy data that showed that local magnetic moments are large on the Cr sites and that moments are essentially absent on the Fe sites. He reported that he measured the magnetic moments on the Cr sites to be between .6 and 2.2 μ_B . Wu et. al. [1] then measured the magnetic susceptibility, shown in Fig. 1.4, thus adding to the knowledge of the magnetic structure. The

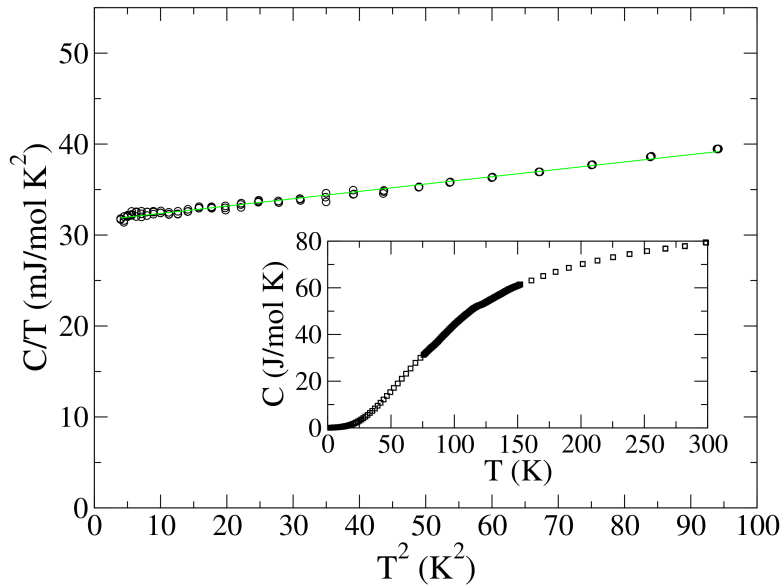


Figure 1.3: Heat capacity of FeCrAs, figure taken with permission from Wu et. al. [1]. Where the plot intercepts the C/T axis is the Sommerfeld coefficient, which here is roughly 31 mJ/mol K^2 . The effective mass associated with the Sommerfeld coefficient of FeCrAs is significantly lower than is seen in the heavy Fermion materials, but it is very large for a d electron material [1].

susceptibility was found to be Pauli-like, and it gives a Wilson ratio of between 4 and 5. The c-axis and the a-axis susceptibilities show a peak around $T_N = 125\text{K}$, signaling the transition to the $\sqrt{3} \times \sqrt{3}$ coplanar antiferromagnetic order.

To achieve the long-term goal of explaining the properties of FeCrAs, we must have a model for the material that contains microscopic physics of FeCrAs. We have achieved the short-term goal of constructing such a model.

1.2 Previous approaches to studying FeCrAs: The insulating perspectives

As the problem of the description of the resistivity of FeCrAs is an open problem, no approaches have been completely ruled out yet, and in the present section, we present

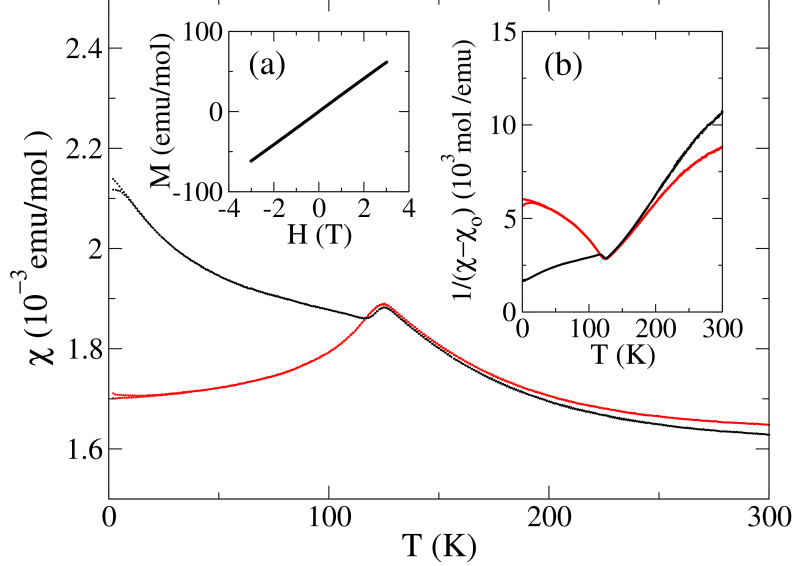


Figure 1.4: Magnetic susceptibility of FeCrAs, figure taken with permission from [1]. The local maximum around $T_N = 125\text{K}$ signals the antiferromagnetic transition as the temperature is lowered. The system orders into a $\sqrt{3} \times \sqrt{3}$ state below T_N . The Wilson ratio given by the susceptibility is between 4 and 5 [1].

some details of the two theories existing prior to our work. Hae-Young Kee's group at University of Toronto proposed two theories for FeCrAs.

One theory, proposed by Redpath et. al. [2], considered a classical antiferromagnetic Heisenberg model between nearest neighbor Cr spins as well as an additional term representing the interaction between classical Cr spins and a spin representing the Fe trimer in FeCrAs. The single spin that represents the Fe trimer resides in the center of the trimer. The Hamiltonian of Redpath et. al. takes the form

$$H = J_1 \sum_{\langle ij \rangle} \vec{s}_i^{Cr} \cdot \vec{s}_j^{Cr} + J_2 \sum_{\langle ik \rangle} \vec{s}_i^{Cr} \cdot \vec{s}_k^{Fe} \quad (1.1)$$

where J_1 is the Cr-Cr exchange and J_2 is the Cr-Fe exchange, while \vec{s}_i^{Cr} is a classical spin moment on the Cr sites and \vec{s}_i^{Fe} is a single classical spin moment representing the spin of the Fe trimer.

Redpath et. al. [2] carried out Monte Carlo simulations on their model in order to find transition temperatures that they used to draw phase boundaries in their phase diagram. They found that for a certain range of values of J_1 and J_2 , there was $\sqrt{3} \times \sqrt{3}$ phase, which is the experimentally observed magnetic state in FeCrAs. So, their finding was that a model with classical moments on sites with geometry similar to FeCrAs gives a $\sqrt{3} \times \sqrt{3}$ state. Therefore, their simple model gives an explanation of the rough magnetic structure of FeCrAs.

In a second theory paper by Rau and Kee [3], the authors try to capture the magnetic structure of FeCrAs by considering a classical model of localized moments interacting with the Fe sublattice via a simple exchange. Due to the uniform character of the relevant trimer states and the assumption of equal exchanges between Cr and different Fe orbitals, the effective exchange between the Cr and the trimers will be equal and between all of the Cr in the surrounding hexagons in the layers above and below [3]. Their Hamiltonian takes the form

$$H = -t \sum_{\langle ij \rangle \in ab} \sum_{\sigma} c_{i\sigma}^{\dagger} c_{j\sigma} - t' \sum_{\langle ij \rangle \in c} \sum_{\sigma} c_{i\sigma}^{\dagger} c_{j\sigma} + U \sum_i n_{i\uparrow} n_{i\downarrow} \\ + \frac{J_K}{2} \sum_{\langle ia \rangle} (c_i^{\dagger} \vec{\sigma} c_i) \cdot \vec{S}_a + J_H \sum_{\langle ab \rangle} \vec{S}_a \cdot \vec{S}_b \quad (1.2)$$

where Fe electron creation and annihilation operators are denoted by $c_{i\sigma}^{\dagger}$, $c_{i\sigma}$, and the classical Cr spins are denoted by \vec{S}_a . The hopping parameters t and t' correspond to hopping processes within the ab plane and along the c-axis, respectively. Fe sites are denoted by i and j while Cr sites are denoted by a and b . $\langle ij \rangle \in ab, c$ denotes bonds in the ab plane or c direction, respectively. Additionally, $\langle ia \rangle$ denotes nearest-neighbor pairs of Cr kagome and Fe trimer sites. U is the intratrimer repulsion, J_K is the Fe-Cr exchange, and J_H is the Cr-Cr exchange [3].

Rau and Kee [3] used slave-rotor mean field theory on Eq. 1.2. The so-called spin

liquid phase in the phase diagram obtained in the paper is a possible route to the non-Fermi liquid physics of FeCrAs.

1.3 Our approaches to the study of FeCrAs and the metallicity spectrum

We seek a model to describe the properties of FeCrAs. A model with hopping electrons and local moments can capture strong correlation physics and magnetism. Perhaps the simplest model that meets these conditions is the Kondo Lattice Model on the kagome lattice. We can study the Kondo Lattice Model on the kagome lattice with the hope that we will make progress in understanding FeCrAs.

$$H_{KLM} = -t \sum_{\langle ij \rangle \sigma} c_{i\sigma}^\dagger c_{j\sigma} + h.c. - \frac{J_K}{2} \sum_{i\sigma\sigma'} \vec{S}_i \cdot \left(c_{i\sigma}^\dagger \vec{\tau}_{\sigma\sigma'} c_{i\sigma'} \right), \quad (1.3)$$

The kagome Kondo Lattice Model is potentially simple to a fault, because it may not capture some of the physics of FeCrAs. FeCrAs is not as ideal as the 2-dimensional kagome Kondo Lattice Model, which has only one orbital that the conduction electron can be in. Therefore, we further investigate the microscopic properties by calculating Local Density Approximation (LDA) and Local Density Approximation with Hubbard repulsion (LDA+U) [21, 22] results, shown in the beginning of chapter 3. These results and Generalized Gradient Approximation (GGA) [23] results from Akrap et. al. [20] exhibit high d-orbital density of states at the Fermi energy as well as low p-orbital density of states at the Fermi energy. These results and our desire to write down a model rooted in the microscopic physics of FeCrAs motivate us to construct the Optimal Overlap Hopping Model (OOHM), which consists of only d-orbital operators and has 30 bands. The form of the OOHM is

$$H_{OOHM} = \sum_{A,B \in Cr, Fe} H_{A-B} + \sum_{A \in Cr, Fe} H_{CF,A} \quad (1.4)$$

where A,B = Fe, Cr. In short, the Optimal Overlap Hopping Model allows hopping from any Fe or Cr to any nearest neighbor Fe or Cr, and it also includes crystal field splitting to enable conduction of electrons around the system.

We consider both the Optimal Overlap Hopping Model and the Kondo Lattice Model on the kagome lattice as starting points for the study of FeCrAs. In chapter 4, we show an example of a mean-field term that is added to the Optimal Overlap Hopping Model, and this term could help describe inelastic neutron scattering data.

Adding interactions to the Optimal Overlap Hopping Model, we have

$$H_{OOHM+int} = H_{OOHM} + H_{int} \quad (1.5)$$

It is constructive to think of the proposed models for FeCrAs as residing on a spectrum of metallicity, as shown in Fig. 1.5. FeCrAs has a resistivity that is not metallic-like or insulating-like but something between these two extremes. Therefore, on the spectrum of metallicity, an appropriate description of the resistivity of FeCrAs would reside somewhere in the center. All approaches to a description of the resistivity of FeCrAs lie somewhere along the spectrum, and one can envision ways to modify existing models to move from one of the extremes toward an appropriate description of FeCrAs. The antiferromagnetic Heisenberg model from Redpath et. al. [2]. contains no electrons, so it is a completely insulating model which shows up on the left side of the spectrum. The Kondo Lattice Model on the kagome lattice contains electrons that couple with classical local spin moments, which means that it is a step in the metallic direction away from the antiferromagnetic Heisenberg model of Redpath et.

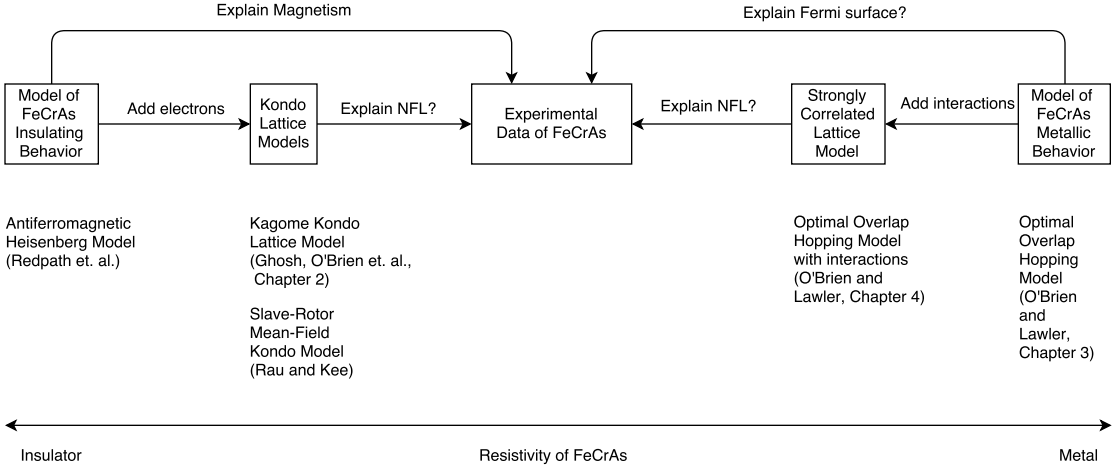


Figure 1.5: Spectrum of metallicity for the theories of FeCrAs. FeCrAs has a resistivity that is not metallic-like or insulating-like but something between these two extremes. Therefore, on the spectrum of metallicity, an appropriate description of the resistivity of FeCrAs would reside somewhere in the center. The antiferromagnetic Heisenberg model from Redpath et. al. [2] contains no electrons, so it is a completely insulating model which shows up on the left side of the spectrum. The Kondo Lattice Model on the kagome lattice contains electrons that couple with classical local spin moments, which means that it is a step in the metallic direction away from the antiferromagnetic Heisenberg model of Redpath et. al. [2]. The proposal of Rau and Kee [3] is also a step in the metallic direction from the insulating side. Rau and Kee's proposal features local Cr moments with the metallic hopping terms. On the metallic side of the spectrum resides the Optimal Overlap Hopping Model. We can add terms to the Optimal Overlap Hopping Model to move the model toward the insulating end of the spectrum, as we do in chapter 4. The Optimal Overlap Hopping Model with interactions added resides in the same part of the spectrum, because with interactions, we can move toward the insulating end of the spectrum.

al. [2]. The proposal of Rau and Kee [3] is also a step in the metallic direction from the insulating side. Rau and Kee's proposal features local Cr moments with the metallic hopping terms.

On the metallic side of the spectrum resides the Optimal Overlap Hopping Model. We can add terms to the Optimal Overlap Hopping Model to move the model toward the insulating end of the spectrum, as we do in chapter 4. The Optimal Overlap Hopping Model with interactions added resides in the same part of the spectrum, because with interactions, we can move toward the insulating end of the spectrum.

One advantage of our method, though, is that it does not change the Hilbert space like the slave-particle method does. All of these models are starting points from which we can launch a study of FeCrAs. It is possible that combinations of all of the proposed models could move one closer to understanding the resistivity of FeCrAs.

Chapter 2

A toy model : The Kondo Lattice Model on the kagome lattice

This chapter, we first motivate a study of the Kondo Lattice Model on the kagome lattice. Next, we talk about the history of the Kondo Lattice Model and what place our work from the present chapter fits into the history. Finally, we will examine the numerics and the phase diagram of the Kondo Lattice Model on the kagome lattice.¹

2.1 Motivation and History - Kondo Lattice Model

We are motivated to study the Kondo Lattice Model (KLM) on the kagome lattice, because FeCrAs seems to have localized moments [15] as well somewhat metallic behavior. The resistivity is low at low temperatures, so even though FeCrAs is a

¹The contents of the present chapter are a result of collaboration with Shivam Ghosh, Michael Lawler, and Chris Henley. Chapter 5 in Shivam Ghosh's PhD thesis describes the kagome Kondo Lattice Model in greater detail than is described here [4]. These results are also the subject of a paper recently published in PRB [5]. The exchange matrices were calculated by Shivam Ghosh. He sent these matrices to the present author, who ran a simulated annealing Monte Carlo algorithm on the exchange matrices to obtain the ground state spin configurations. These ground states were used by Shivam Ghosh to construct the phase diagram as a function of filling fraction and exchange coupling.

strange metal, we will present a simple model, called the Kondo Lattice Model, that contains localized moments as well as metallic behavior. The KLM [24–28] is a model that couples an itinerant electron to classical spin moments that reside on each site of a given lattice. We consider this model here

$$H_{KLM} = -t \sum_{\langle ij \rangle \sigma} c_{i\sigma}^\dagger c_{j\sigma} + h.c. - \frac{J_K}{2} \sum_{i\sigma\sigma'} \vec{S}_i \cdot \left(c_{i\sigma}^\dagger \vec{\tau}_{\sigma\sigma'} c_{i\sigma'} \right), \quad (2.1)$$

where t is the hopping amplitude, $\sum_{\langle ij \rangle}$ is the sum over i and j such that i and j are nearest neighbors, $c_{i\sigma}^\dagger$ ($c_{i\sigma}$) creates (destroys) an electron with spin σ at site i , J_K is the Kondo coupling between the classical moments and an itinerant electron, \vec{S}_i is a classical spin moment residing on site i , and $\vec{\tau}$ is the vector of Pauli matrices.

The KLM [29] is one of the frustrated magnetic systems, which have received a great deal of attention in recent years [11, 26, 30–47]. Frustrated magnetic systems feature localized magnetic moments which interact through competing exchange interactions that cannot be simultaneously satisfied. As a result, a frustrated magnetic system has a large ground state degeneracy [48].

In 1977 Doniach [49] wrote the seminal paper on the KLM. The model that Doniach conceived was one where local spin moments on each site of a lattice were allowed to couple with electrons. He was interested in the phase diagram that resulted from the quantum spins residing on the lattice. We are more interested in analogous models with classical spins residing on the lattice. Geometric frustration is our focus. The rest of the literature we discuss are classical Kondo Lattice Models.

A great deal of interest has also been shown in the pyrochlore lattice, which is the lattice of corner sharing tetrahedra. A great deal of work has been done to find the ground state of the KLM on the pyrochlore lattice [28]. Most of the states considered for the pyrochlore lattice are the so-called spin ice states [32, 50, 51].

Martin and Batista [24] considered the KLM on the triangular lattice in 2008. They found “tetrahedral” magnetic order commensurate with a quadrupled unit cell at $\frac{1}{4}$ filling fraction. The discovery of non-coplanar order was the first example of its kind in the context of the KLM. In 2010, Kato, Martin, and Batista [52] built upon the work of Martin and Batista by studying the $1/4$ filled KLM in more detail, combining a zero-temperature variational approach with finite-temperature Monte Carlo simulations. The same year, Akagi and Motome [25] also studied the KLM on the triangular lattice, focusing on the spin chirality of the states and the anomalous hall effect. In 2013, Akagi and Motome [53] published a paper presenting the phase diagram for the KLM for the triangular-to-kagome lattice. The triangular-to-kagome lattice has a hopping parameter, t' , to hop to sites that exist in the triangular lattice but not the kagome lattice. As t' is tuned from being the same value as the other hopping parameter to 0, the lattice changes from triangular to kagome.

In 2014, Barros et. al. [54] considered the Kondo-lattice model on the kagome lattice. They considered the filling fractions of $1/4$ and $5/12$ and found many non-coplanar orders. Around the same time, we published our paper on arxiv (later published in PRB [5]), and we found numerous incommensurate orders in addition to agreeing with the results of Barros et. al. [54]. Since our work was published, Sung and Lawler [55] published a paper about using the Berry flux as an order by disorder decision maker for the kagome KLM states.

In addition to the interest in the KLM for the purposes of further understanding solid state physics, there has also been interest in KLM in cold atoms [56, 57]. These studies have the potential to be interesting, as the context of cold atoms often provides excellent testing grounds for these kinds of models.

2.2 A simple motivation for the Kondo Lattice Model on the kagome lattice

In the present section we use the chemistry and geometry of FeCrAs to motivate a Kondo Lattice Model on the kagome lattice. We start by considering the electron configurations

$$\begin{aligned} Fe &: [Ar]4s^23d^6 \\ Cr &: [Ar]4s^13d^5 \\ As &: [Ar]4s^23d^{10}4p^3 \end{aligned} \tag{2.2}$$

Arsenic is highly electronegative, so we assume that the As atoms will have filled shells. We also assume that the Fe and Cr atoms will shed their 4s electrons. This gives the oxidation states

$$\begin{aligned} Fe\ 2+ &: [Ar]3d^6 \\ Cr\ 1+ &: [Ar]3d^5 \\ As\ 3- &: [Kr] \end{aligned} \tag{2.3}$$

We use the oxidation state of As to calculate a crystal field splitting diagram for the energy of the Cr atoms. Then, we use the Cr oxidation state to fill the Cr splitting diagram with electrons, obtaining many-body states. A crystal field Hamiltonian [58] splits the degenerate energy levels of a free space atom. The crystal field Hamiltonian has the form

$$H_{CF} = \sum_i \frac{kQe}{\sqrt{|\vec{r}_i - \vec{R}_i|^2 + t^2}}, \quad (2.4)$$

where \sum_i denotes the sum over vertices of the polyhedron of As atoms that surrounds a Cr atom, k is Coulomb's constant, Q is the charge on each vertex, e is the charge of the electron, R_i is the distance of the vertex, i, from the origin, where the Cr atom resides, and t is a softening parameter used to remove the singularities when we integrate. In the case we are considering, Q = -3e on the As sites.

We express the matrix elements of the crystal field Hamiltonian in the basis of the d electron wavefunctions and diagonalize the matrix to find the corrections to the free space d electron wavefunction energies.

$$H_{CF}^{mm'} = \int d^3r \psi_{32m}^* H_{CF} \psi_{32m'} \quad (2.5)$$

$$= \int d^3r \psi_{32m}^* \sum_i \frac{kQe}{\sqrt{|\vec{r}_i - \vec{R}_i|^2 + t^2}} \psi_{32m'}, \quad (2.6)$$

where ψ_{32m} is a hydrogenic wavefunction with n = 3 and l = 2. We choose these particular hydrogenic wavefunctions because Cr atoms have 3d electrons in their valence. In order to find the crystal field splitting energies, we must find the matrix, H_{CF} , given by Eq. (2.6) for m, m' = -2...2, and then we must diagonalize H_{CF} .

In chapter 1, we mentioned that As atoms pyramidal coordinate Cr atoms. For the pyramidal case, we calculate the matrix from Eq. (2.6) and find the eigenvalues, called the crystal field splitting energies. We make diagrams to show the degeneracies and states that result from calculating the crystal field splitting energies. The results for the pyramidal splitting of the Cr levels due to As are shown in Fig. 2.1.

The line on the left of the splitting diagram represents the degenerate energy that

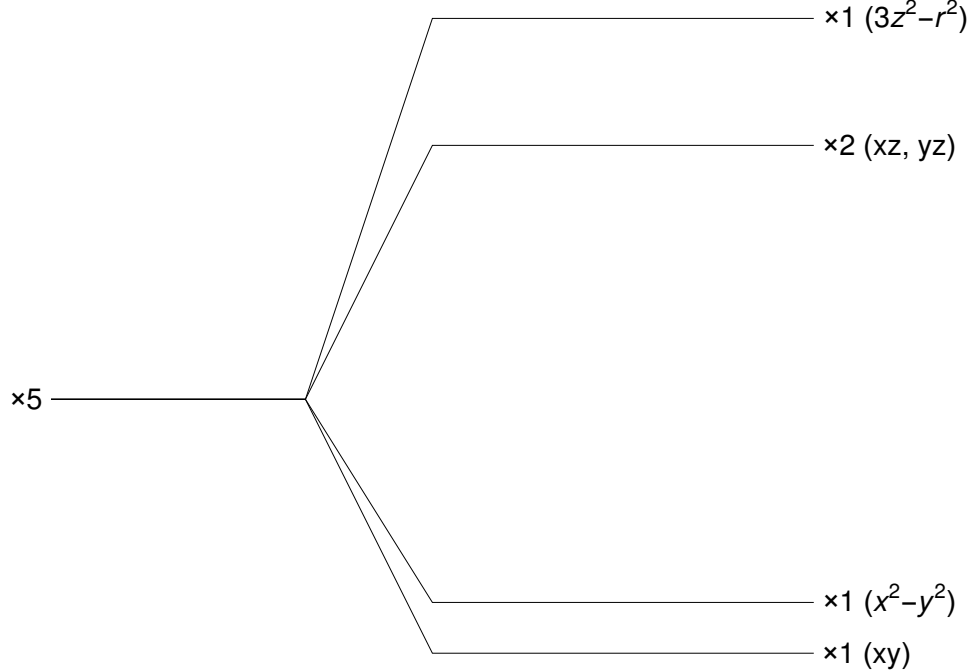


Figure 2.1: The Cr sites are pyramidally coordinated by As sites in FeCrAs. We calculate non-ideal pyramidal crystal field splitting levels of the d electrons on the Cr sites. The degeneracies of the energy levels and the associated states are shown on the right. The most important result of this calculation is that the $3z^2 - r^2$ is the highest energy state. This fact becomes useful when considering the hopping model that results from placing these $3z^2 - r^2$ orbitals on the kagome lattice. This hopping model has only one hopping parameter because all pairs of these azimuthally symmetric $3z^2 - r^2$ orbitals are equally spaced, so their overlap integrals are all the same.

all orbitals have in free space. Once we apply the field from the As atoms, these degenerate states split into a lower degeneracy represented by the lines on the right.

Fig. 2.1 shows the results for the pyramidal splitting of the Cr levels due to As.

These splitting diagrams are single-particle energy spectra that we fill with electrons. Each distinct way that we fill these diagrams with electrons gives a distinct many-body state. Here, we consider two of extreme cases. In one case, called the high-spin case, we fill the energy levels with as many up spins as possible. In Fig. 2.2, we show the high spin case for Cr.

The high spin case for Cr is suggestive; it resembles the KLM on the kagome

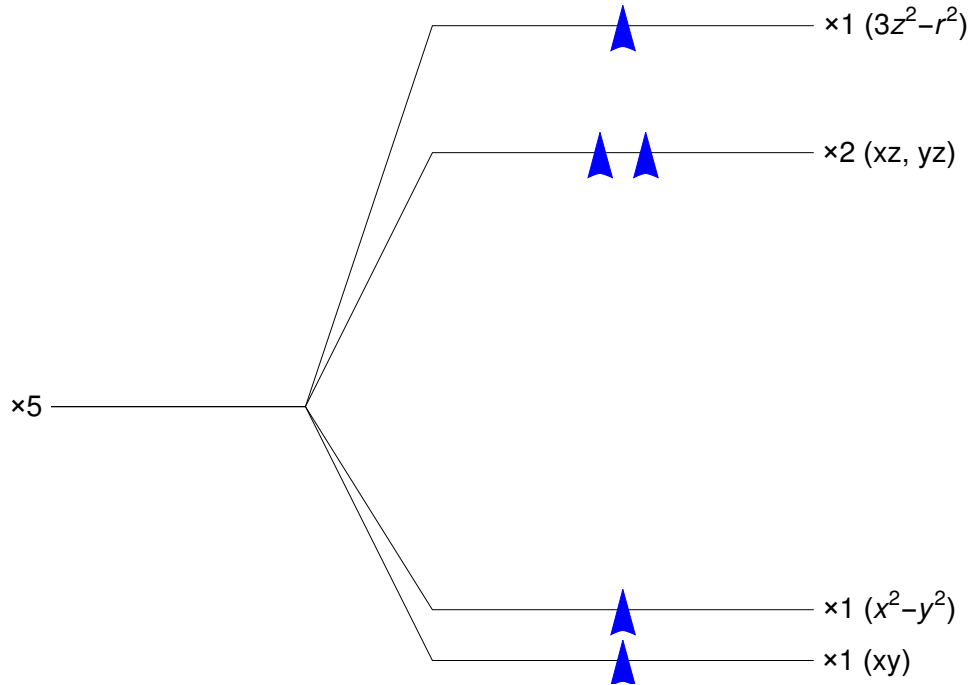


Figure 2.2: After calculating crystal field splitting diagrams, we fill the energy levels with the electrons available for Cr and Fe. Since we have assumed a Cr 2+ oxidation state, we have 6 electrons to place in the Cr splitting diagram. We fill the diagram assuming the high spin case, which assumes that the energy level spacings are smaller than the intraorbital Coulomb repulsion.

lattice. If we draw a “bubble” around the bottom 4 spins, we lump these 4 spins into a classical core spin moment. The classical moment and the top (itinerant) electron in the energy diagram now resemble the essential pieces that we see in the KLM. The definition of the classical moment is shown in Fig. 2.3. If we consider that we have a lattice of these Cr sites, and we allow itinerant electrons to hop from one Cr site to another in the conduction band. This is the toy KLM we considered at the beginning of the chapter. The highest energy level in this Cr splitting diagram is the $3z^2 - r^2$, which is an orbital that has azimuthal symmetry in the x-y plane. Therefore, directionality does not affect hopping parameters that one may calculate by considering the overlap of one $3z^2 - r^2$ orbital with another in the kagome plane. All of the hopping parameters only depend on the distance between the orbitals, and

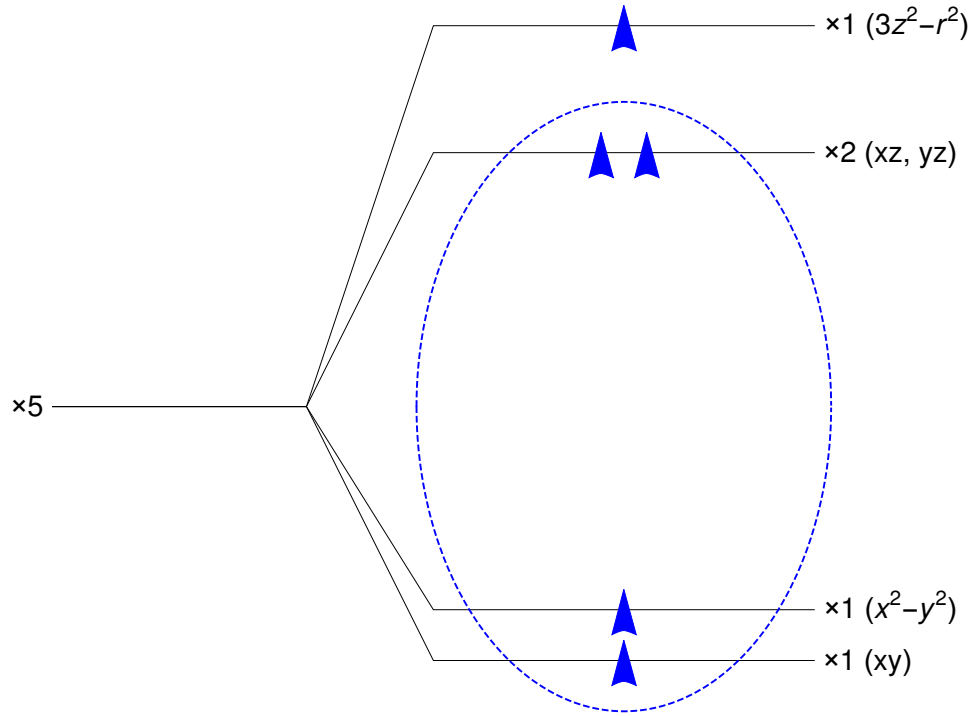


Figure 2.3: To create a toy model, we observe that the high spin case for the crystal field splitting calculated has a single electron in the highest energy level. We make a crude approximation that this electron in the highest energy level is an itinerant electron and that the bottom four electrons form a classical moment. We are motivated to call these bottom 4 electrons a classical moment because experiment has shown that the magnetic moment on the Cr sites be anywhere from 0.6 to $2.2 \mu_B$, and the classical moment that we have here is $2.0 \mu_B$. We then allow the itinerant electron to couple with the classical moment. This interaction along with a hopping term is the KLM.

all of the hopping parameters are the same value.

2.3 Phase diagram of the Kondo Lattice Model on the kagome lattice

Here, we study the energetics of the Kondo Lattice Model on the kagome lattice. Using perturbation theory, we make progress in learning about the KLM, ultimately finding the phase diagram of the kagome KLM. The perturbative limit we consider is $t \ll J_K$, which is called the RKKY limit, because the model that results is called the Ruderman-Kittel-Kasuya-Yosida model [59–61]. In the RKKY limit, the unperturbed Hamiltonian in Eq. 2.1 is the hopping term

$$H_0 = -t \sum_{\langle ij \rangle \sigma} c_{i\sigma}^\dagger c_{j\sigma} + h.c. \quad (2.7)$$

and our perturbation Hamiltonian is the Kondo term

$$H_1 = \frac{J_K}{2} \sum_i \vec{S}_i \cdot \left(c_{i\sigma}^\dagger \vec{\tau}_{\sigma\sigma'} c_{i\sigma'} \right) \quad (2.8)$$

When we calculate the single-particle energy spectrum of the unperturbed Hamiltonian, there are degenerate blocks of energies. We find non-degenerate ground state energies by summing up the energies in the spectrum to the end of these degenerate blocks. Because the ground state we found is non-degenerate, we can calculate energy corrections in non-degenerate perturbation theory.

The first order correction is zero, because the ground state, $|G\rangle$, of the unperturbed Hamiltonian is one where we have filled up each energy with a spin up and spin down electron. $|G\rangle$ has rotational invariance. The spin operator in the Kondo term also has rotational invariance, so the expectation value of the Kondo term in the ground state of the hopping term is zero.

The second-order correction is

$$E_G^{(2)} = \frac{J_K^2}{4} \sum_m - \frac{\langle G | \sum_i \vec{S}_i \cdot (c_{i\sigma}^\dagger \vec{\tau}_{\sigma\sigma'} c_{i\sigma'}) | m \rangle \langle m | \sum_j \vec{S}_j \cdot (c_{j\sigma}^\dagger \vec{\tau}_{\sigma\sigma'} c_{j\sigma'}) | G \rangle}{E_G - E_m} \quad (2.9)$$

where $|G\rangle$ denotes the ground state of the unperturbed Hamiltonian, and $|m\rangle$ denotes any single-particle excited state in the unperturbed model.

We transform the real space Fermion operators into the eigenbasis using

$$c_{Rd}^\sigma = \mathcal{U}_{Rk} \mathcal{U}_{d\lambda}^k c^{k\lambda\sigma} \quad (2.10)$$

where \mathcal{U}_{Rk} is the Fourier factor and $\mathcal{U}_{d\lambda}^k$ is the matrix that diagonalizes the 3x3 hopping matrix at a given point k . This gives us

$$E_G^{(2)} = \frac{J_K^2}{4} \sum_m \frac{\langle G | A | m \rangle \langle m | \tilde{A} | G \rangle}{E_G - E_m} \quad (2.11)$$

where

$$A = c^{k\lambda\sigma\dagger} \mathcal{U}_{\lambda d}^{k\dagger} \mathcal{U}_{kR}^\dagger \tau_{\sigma\sigma'}^\alpha \mathcal{U}_{Rk'} \mathcal{U}_{d\lambda'}^{k'} c^{k'\lambda'\sigma'} \quad (2.12)$$

and

$$\tilde{A} = c^{\tilde{k}\tilde{\lambda}\tilde{\sigma}\dagger} \mathcal{U}_{\tilde{\lambda}d}^{\tilde{k}\dagger} \mathcal{U}_{\tilde{k}\tilde{R}}^\dagger \tau_{\tilde{\sigma}\tilde{\sigma}'}^\beta \mathcal{U}_{\tilde{R}\tilde{k}'} \mathcal{U}_{\tilde{d}\tilde{\lambda}'}^{\tilde{k}'} c^{\tilde{k}'\tilde{\lambda}'\tilde{\sigma}'} \quad (2.13)$$

and we have used 4 sets of labels on which we find conditions. The only non-zero contributions are those where the system starts in the ground state, gets excited

to a single-particle excited state, then returns to the ground state. The resulting expression is

$$E_G^{(2)} = \frac{J_K^2}{4} \sum_{k\lambda, \epsilon_{k\lambda} < \epsilon_F} \sum_{k'\lambda', \epsilon_{k'\lambda'} > \epsilon_F} \sum_{R\tilde{R}dd} S_{Rd}^\alpha S_{\tilde{R}\tilde{d}}^\beta \frac{\mathcal{U}_{\lambda d}^{\dagger k} \mathcal{U}_{kR}^\dagger \tau_{\sigma\sigma'}^\alpha \mathcal{U}_{Rk'} \mathcal{U}_{d\lambda'}^{k'} \mathcal{U}_{\lambda' \tilde{d}}^{\dagger k'} \mathcal{U}_{k' \tilde{R}}^\dagger \tau_{\sigma'\sigma}^\beta \mathcal{U}_{\tilde{R}k} \mathcal{U}_{\tilde{d}\lambda}^k}{\epsilon_{k\lambda} - \epsilon_{k'\lambda'}} \quad (2.14)$$

In Eq. (2.14), the k and λ associated with the last two unitary matrices are fixed to the k and λ associated with the first two unitary matrices. Also, we have calculated the dot product in each of the factors in the numerator of Eq. (2.9). Since the corrections to the energy must be real, we are left with the condition that $\alpha = \beta$. The resulting formula is

$$H = \sum_{ij} J_{ij} \vec{S}_i \cdot \vec{S}_j \quad (2.15)$$

where

$$J_{ij} = \frac{3J_K^2}{4} \sum_{k\lambda, \epsilon_{k\lambda} < \epsilon_F} \sum_{k'\lambda', \epsilon_{k'\lambda'} > \epsilon_F} \sum_{R\tilde{R}dd} \frac{\mathcal{U}_{\lambda d}^{\dagger k} \mathcal{U}_{kR}^\dagger \mathcal{U}_{Rk'} \mathcal{U}_{d\lambda'}^{k'} \mathcal{U}_{\lambda' \tilde{d}}^{\dagger k'} \mathcal{U}_{k' \tilde{R}}^\dagger \mathcal{U}_{\tilde{R}k} \mathcal{U}_{\tilde{d}\lambda}^k}{\epsilon_{k\lambda} - \epsilon_{k'\lambda'}} \quad (2.16)$$

Here \vec{S}_i is a classical spin on the kagome lattice, and J_{ij} is the exchange matrix, which describes the interaction between the classical spins in Eq. 2.15. In our paper, we show the first four exchange parameters plotted as a function of electron filling [4, 5]. Fig. 2.4 shows the plot of the exchange parameters.

The opposite limit, $t \gg J_K$, is called the double exchange limit [62–64]. The dominant phase in the double exchange limit is the ferromagnetic state. We can see that the various exotic as well as the more well-known coplanar antiferromagnetic

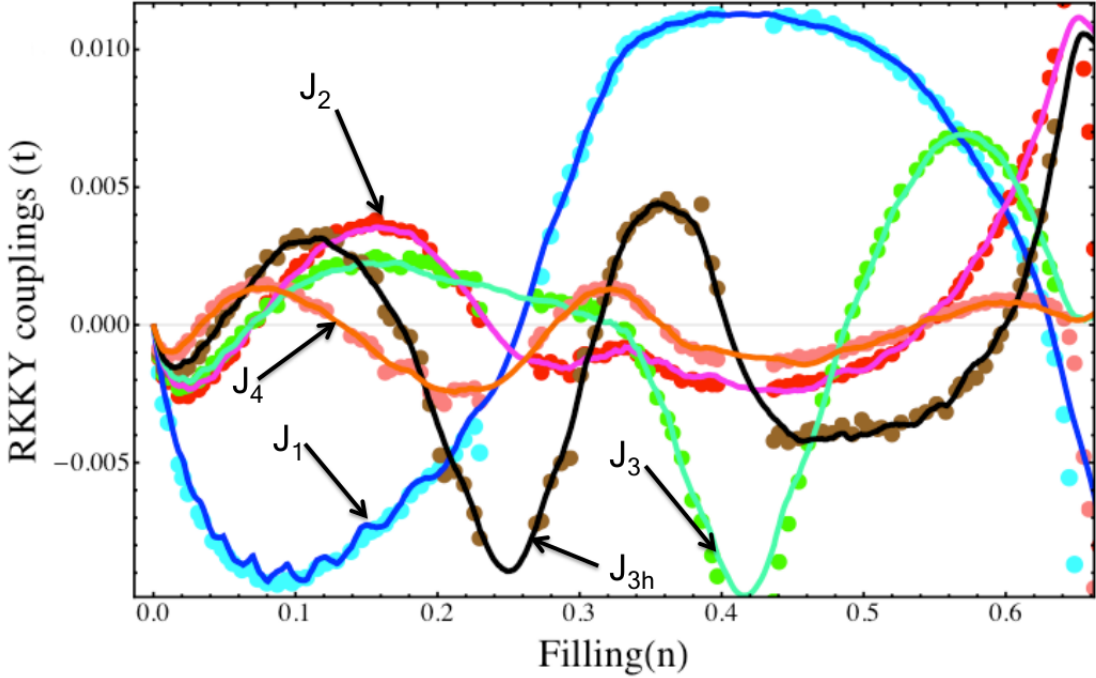


Figure 2.4: Calculated exchange couplings in the RKKY limit. The first four couplings are plotted as a function of filling fraction in units of $\frac{J^2}{t}$. The plotted points result from second-order perturbation, as detailed in the text. J_1 is the nearest neighbor exchange coupling, J_2 is the next-nearest neighbor exchange coupling, and J_3 and J_{3h} are two types of next-next-nearest exchange coupling, with J_{3h} being the coupling associated with pairs of sites on opposite sides of a hexagon. The curves are the result of a fitting procedure explained in chapter 5 of Shivam Ghosh's PhD thesis. Figure from [4]

phases become less prevalent as J_K is increased [5, 53]. We are not as concerned with the double exchange limit, because we seek the interesting and exotic phases that prevail in the RKKY limit.

A given matrix depended on system size, $N_1 \times N_2 \times 3$ number of sites, as well as filling fraction, n. For a given matrix, we calculate the ground state spin configuration and its energy using a classical Monte Carlo-based [65] simulated annealing algorithm. We detail the simulated annealing procedure here.

1. Generate a random spin configuration of N_{sites} numbers of unit-length spins.
2. Calculate the energy of the random initial spin configuration with Eq. (2.15).

3. Randomly choose a spin out of the spin configuration. In other words, choose a random number between 1 and N_{sites} , and the number now labels the spin of interest.
4. Flip the spin chosen in the previous step. We choose to randomly select a spin that is within a certain angle of the spin of interest.
5. Once the spin has been flipped, we have an old spin and a new spin. We calculate the change in energy between the old spin configuration (the spin configuration that contains the old spin) and the new spin configuration (the spin configuration that contains the new spin). The change in energy is $\Delta E = \sum_i (\vec{S}_{new} - \vec{S}_{old}) \cdot \vec{S}_i$.
6. If $\Delta E < 0$, it means the energy is lowered. If the energy is lowered, it means we are moving toward the ground state, therefore we keep the spin flip. If $\Delta E > 0$, we compare the Boltzmann factor, $e^{-\frac{\Delta E}{k_B T}}$, to a randomly chosen number, n_{rand} between 0 and 1. If n_{rand} is less than the Boltzmann factor, we also accept the spin flip. If the random number is larger than the Boltzmann factor, the spin flip is rejected.
7. We iterate until we are certain that the result has converged. The number of iterations is usually roughly 1,000,000 - 2,000,000.
8. We accept 50% of the total spin flips, because a 50% acceptance rate ensures proper convergence of our results.
9. After the energy and acceptance rate converge, we lower the temperature in the Boltzmann factor, and repeat steps 3-8 with the currently stored spin configuration.
10. Continue to lower the temperature until lowering the temperature does not lower the energy further. We calculated autocorrelation time [66] at each tem-

perature to inform us about how many iterations we should calculate at each temperature. Moving to the next (lower) temperature prematurely may cause the system to freeze into the incorrect order, preventing us from finding the ground state energy of the system. As we lower the temperature, the system goes through a phase transition if we have run a sufficient number of iterations. Once the system goes through the phase transition, we don't need to worry about freezing in the incorrect order.

11. The whole process of lowering the temperature and settling to a new state is called simulated annealing.

After we have a functional Monte Carlo code to find the ground state spin configuration of our systems, we run this code on systems of different size and filling fraction, and we find states that have a so-called incommensurate order. Incommensurate order is when the pattern of the spins does not "fit nicely" into the system size. In Fig. 2.5 we show a common-origin plot [45, 67] of the spins that result from running Monte Carlo on the 9x9 exchange tensor (near half filling).

Using the Monte-Carlo simulated annealing technique we identify several states in the limit $J_k \ll t$. Using these same states, we generate a variational phase diagram for arbitrary values of $\frac{J_k}{t}$. To clarify, the energies of the states that we find at small $\frac{J_k}{t}$ are calculated at arbitrary values of $\frac{J_k}{t}$ and filling, n , and the given arbitrary point is colored with the color that corresponds to a particular state. We show the variational phase diagram in Fig. 2.6 [5].

In the phase diagram at half filling and small $\frac{J_k}{t}$, three states compete to be the most energetically favorable. One state is $\sqrt{3} \times \sqrt{3}$, another is a state called cuboc1 [26], and the third is an incommensurate state like the one that we found using Monte Carlo, as shown in Fig. 2.5. That these state are all competing at intermediate values of $\frac{J_k}{t}$ is interesting, as it has been found experimentally that one of these coplanar 120 degree states, the $\sqrt{3} \times \sqrt{3}$ state, is likely the ground state below 125K [1].

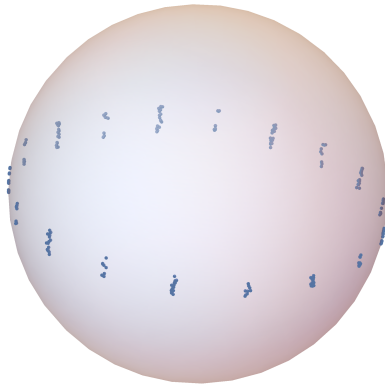


Figure 2.5: We find the ground state for the KLM of a given Kondo exchange coupling and filling fraction. We use the exchange tensor, which is calculated in the RKKY limit, to calculate the change in energy for each iteration of the Monte Carlo algorithm. This change in energy is used to define a Boltzmann factor used in the decision criterion of each Monte Carlo iteration (see simulated annealing procedure in text). The plot here is a common-origin plot of the ground state spin configuration resulting from simulated annealing for the 9 unit cell \times 9 unit cell system size at filling fraction of roughly $n = .5$.

Though this model is quite simple in form, its complexity gives us hope that it may be capturing at least some of the physics of FeCrAs.

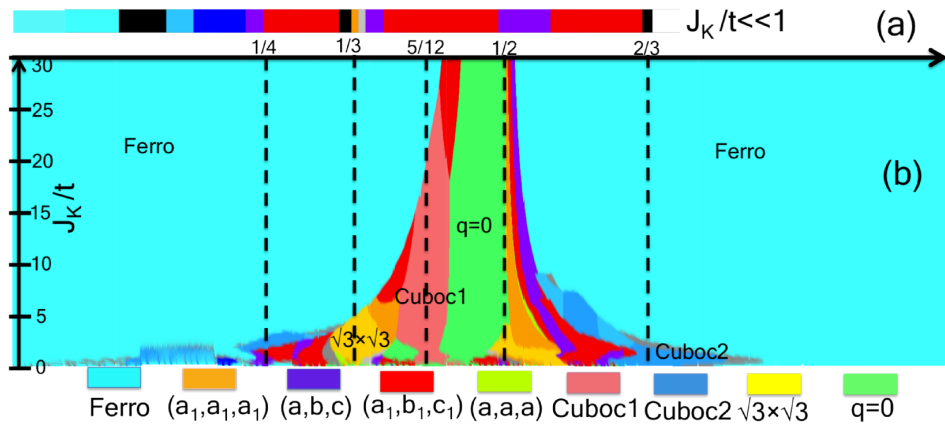


Figure 2.6: Variational phase diagram for the KLM in the (n, J_K) plane, with the filling range $n = (0,1)$ and the Kondo coupling range $J_K = [0,8]$. The points calculated along the J_K direction have spacings of $0.05t$. The colored strip at the bottom is the RKKY phase diagram as a function of n , with the same color convention as the phases above. From [5].

Chapter 3

Optimal Overlap Hopping Model

We seek to describe the magnetic structure, the resistivity, and the lack of superconductivity in FeCrAs. The other approach we considered, the kagome KLM, had a tenuous connection with the microscopic physics of FeCrAs. Here, we construct and study a tight binding model for FeCrAs, motivated by the microscopic physics of FeCrAs. First, we present DFT data for FeCrAs. The common features of these DFT calculations, namely the band character, motivate us to consider an effective hopping model consisting of exclusively d-orbitals, called the Optimal Overlap Hopping Model. We then express the effective hopping model in a general form. Then we use the geometry of FeCrAs to express the effective hopping terms in more detail. Subsequently, we derive the form of the effective hopping terms by fitting an effective hopping model to a cluster model. Finally, we calculate a band structure of the Optimal Overlap Hopping Model.¹

¹We acknowledge our collaboration with Turan Birol for the present chapter. Turan calculated all LDA and LDA+U band structures for FeCrAs.

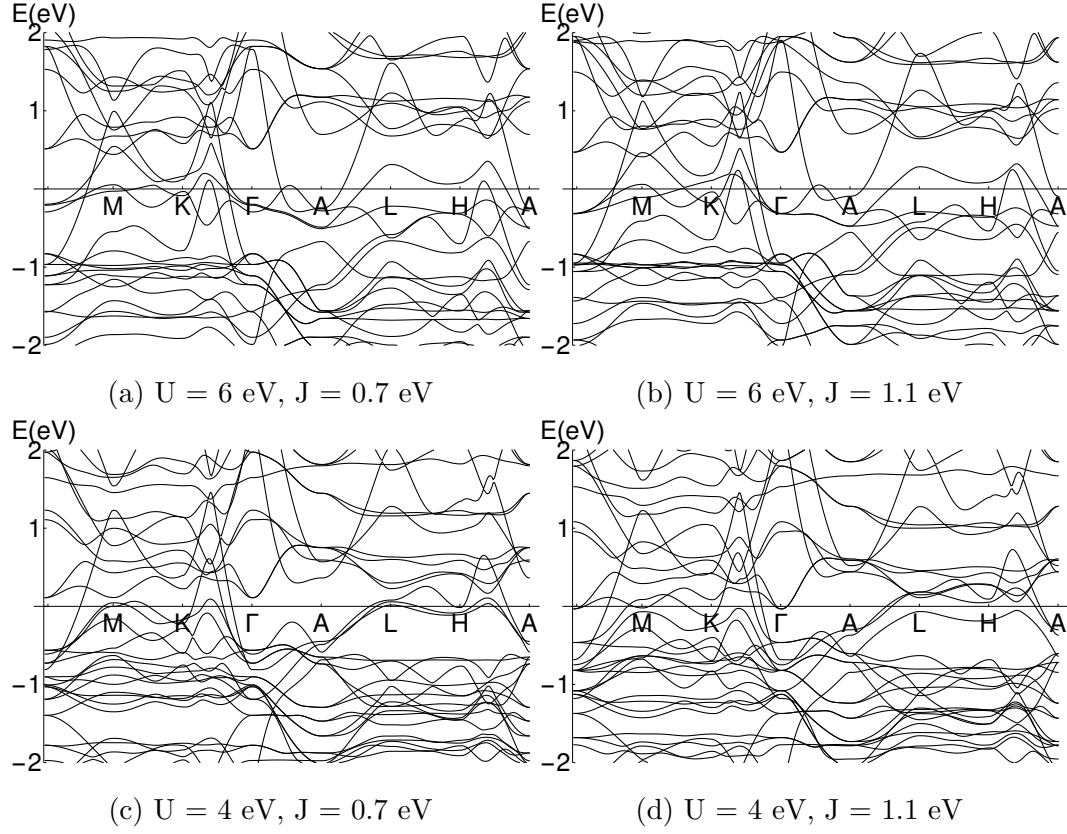
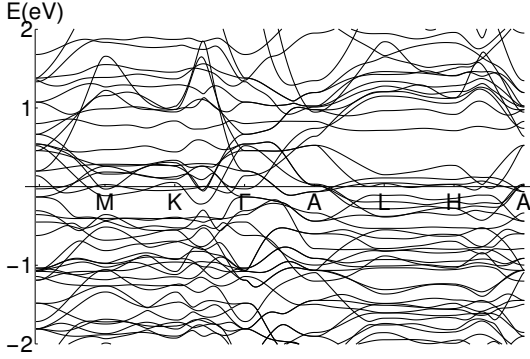


Figure 3.1: The DFT results were obtained with VASP, version 5.2. The energy cutoff for the plane waves was 500 eV. The program uses the projector augmented plane wave method [6]. We used a Monkhorst-pack grid of 1 k-point per 0.3 \AA^{-1} in the reciprocal space. In addition to these settings, we also used $U = 4 \text{ eV}$ and 6 eV and $J = 0.7 \text{ eV}$ and 1.1 eV to obtain the four plots shown in Fig. 3.10. The plots here have been arranged with increasing J to the right and increasing U upward. We see that the plots are sensitive to changes in U , while the plots are not as sensitive to J . The band structures are plotted along the $\Gamma\text{-M}\text{-K}\text{-}\Gamma\text{-A}\text{-L}\text{-H}\text{-A}$ path.

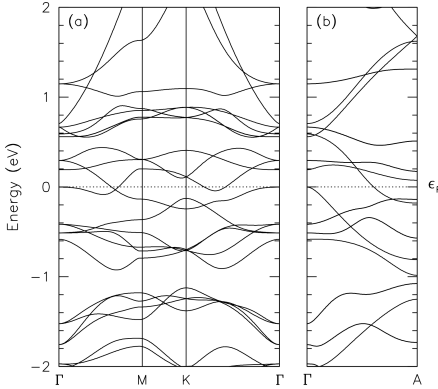
3.1 DFT Results for FeCrAs

We have calculated LDA and LDA+U band structure results for FeCrAs. Akrap et al. [20] have calculated GGA results as well. These three electronic structure results all look quite different. We use information that is common among these calculations. For example, each of these calculations have a high density of Cr and Fe bands around the Fermi energy, while As has low band density around the Fermi energy.

The DFT results were obtained with VASP, version 5.2. The energy cutoff for



(a) LDA calculation of the band structure of FeCrAs. The LDA calculation is obtained in the same way as the LDA+U results, except for this result, both $U=0$ and $J=0$.



(b) Electronic structure calculations “within the generalized gradient approximation (GGA) using the full-potential linearized augmented plane-wave (FP-LAPW) method with local-orbital extensions in the Wien2k implementation.”, figure taken with permission from [20]. The band structure for a high-symmetry path in the hexagonal Brillouin zone’s a) k_x, k_y plane and b) k_z plane. Two bands cross the Fermi energy.

Figure 3.2: The LDA and the GGA calculations. As a first attempt to compare the DFT results, we can compare the Γ point degeneracies with the hope of identifying similarities in the bands.

the plane waves was 500 eV. The program uses the projector augmented plane wave method [6]. We used a Monkhorst-Pack grid of 1 k-point per 0.3 \AA^{-1} in the reciprocal space. In addition to these settings, we also used $U = 4 \text{ eV}$ and 6 eV and $J = 0.7 \text{ eV}$ and 1.1 eV to obtain the four plots shown in Fig. 3.10. The plots in Fig. 3.10 have been arranged with increasing J to the right and increasing U upward. We see that the plots are sensitive to changes in U , while the plots are not as sensitive to J .

While these DFT calculations seem quite different from one another, we can, nonetheless, compare certain aspects of these band structures. One aspect that we

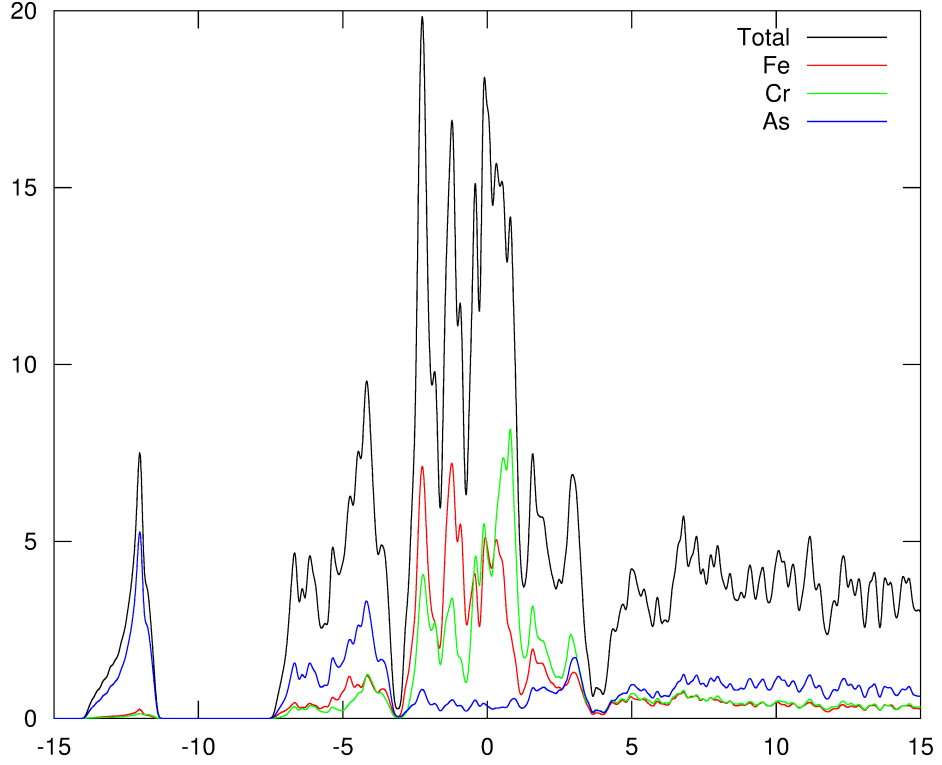


Figure 3.3: Band character for band structure calculated in the LDA. The As bands have very low density at the Fermi energy, while the Cr and Fe bands are dense at the Fermi energy. We use the band character information to justify writing an effective hopping model with only d-electron operators. The band character calculation for the LDA band structure shown here was done by Turan Birol [7].

can compare is the degeneracy of the bands at the Γ point. In the GGA calculation at the Γ point, one singly-degenerate band is at the Fermi energy, a second singly-degenerate band is around .2 eV, a doubly-degenerate band is at .3 eV, and another doubly-degenerate band is at -.4 eV. In summary, the GGA calculation has singly-degenerate bands near the Fermi energy at the Γ point. The LDA calculation also has singly-degenerate bands near the Fermi energy at the Γ point. The LDA+U calculations in general have doubly degenerate bands close to the Fermi energy, unlike the GGA calculation.

Despite the complicated nature of the DFT results, we can still glean constructive information from the results. We calculated the band character of the LDA band

structure, and Akrap et. al. [20] also calculated the band character of their GGA structure, and both band characters showed the same features. In particular, the As bands are well below the Fermi energy, while the Cr and Fe d-electron bands are highly concentrated at the Fermi energy, as shown in Fig. 3.3. The LDA and GGA band character calculations thus motivate us to study an effective model consisting only of d-orbital operators. We call our effective model the Optimal Overlap Hopping Model (OOHM).

3.2 Constructing the Optimal Overlap Hopping Model(OOHM)

Having motivated writing down the OOHM, we proceed by presenting the general form of the model. Next, we express a more explicit form of the OOHM, and, finally, we derive its form.

3.2.1 General form of the OOHM

The OOHM contains hopping processes from any Fe or Cr site to any Fe or Cr site, as well as crystal field splitting terms on both the Fe and Cr sites. Thus, the general form of the OOHM is

$$H_{OOHM} = \sum_{A,B \in Cr,Fe} t_{eff} d_A^\dagger d_B + \sum_{A \in Cr,Fe} H_{CF,A} \quad (3.1)$$

where d_A and d_B are optimal overlap d-orbitals on $A \in Fe,Cr$ and $B \in Fe,Cr$, respectively, and $H_{CF,A}$ is a crystal field Hamiltonian on site $A \in Fe,Cr$. $t_{eff} = t \cos(\theta_{AB})$, where θ is the bond angle associated with a hopping process of an electron that hops from B to A. H_{OOHM} denotes the optimal-overlap hopping model Hamil-

tonian, to which we will add magnetic terms later in the present chapter. In the following sections we will show the exact form of the effective hopping term. In the following sections, we will go through how we find these optimal overlap d-orbitals as well as how we find t_{eff} , which is proportional to $\cos(\theta)$.

3.2.2 Explicit form of the OOHM

Here, we show explicitly the different types of hoppings allowed for each of the general types of hoppings. For the Cr-Cr hopping term, we have

$$H_{Cr-Cr} = t_{A,Cr,eff} \sum_{ij} d_{i,a}^\dagger d_{j,a} + t_{z,Cr,eff} \sum_{ib} d_{i,b}^\dagger d_{i+a_3,\bar{b}} \\ + t_{in,Cr,eff} \sum_{ijb} d_{i,b}^\dagger d_{j,\bar{b}} + t_{out,Cr,eff} \sum_{ij} d_{i,b}^\dagger d_{j,\bar{b}} + h.c., \quad (3.2)$$

where A is the apex of the pyramid of As atoms that coordinate Cr, b = {R+, R-, L+, L-} denote the bonds that Cr makes with the As atoms in the base of the pyramid that coordinates Cr. Also, here we have $\bar{b} = \{R-, R+, L-, L+\}$. Fig. 3.4 shows these bonds along with the associated hopping parameters.

For the Fe-Fe sector we have

$$H_{Fe-Fe} = t_{z,Fe,eff} \sum_{ijc} d_{i,c}^\dagger d_{j,\bar{c}} + t_{out,Fe,eff} \sum_{ijc} d_{i,c}^\dagger d_{j,\bar{c}} + t_{in,Fe,eff} \sum_{ijc'} d_{i,c'}^\dagger d_{j,c'} + h.c., \quad (3.3)$$

where c = {z+, z-} and c' = {L, R}. Fig. 3.5 shows these bonds and associated hopping parameters.

For the Cr-Fe sector we have

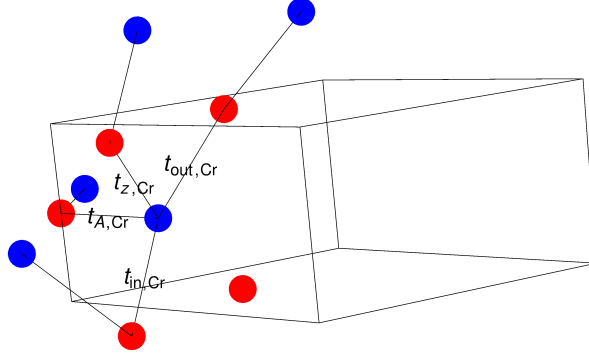


Figure 3.4: Bond types that link a Cr to a neighboring Cr. Blue dots represent Cr atoms, while red dots represent As atoms. There are 4 distinct types of hopping connecting a Cr site to a neighboring Cr site. The wireframe shown is the parallelogram unit cell.

$$H_{Cr-Fe} = t_{Cr-Fe,eff} \sum_{ij} \left(\sum_f d_{i,f}^\dagger d_{j,R} + \sum_{f'} d_{i,f'}^\dagger d_{j,L} \right) + t'_{Cr-Fe,eff} \sum_{i\beta c} d_{i,a}^\dagger d_{j,c} + h.c., \quad (3.4)$$

where $f = \{R+, R-\}$ and $f' = \{L+, L-\}$. Fig. 3.6 shows these bonds and associated hopping parameters.

When hopping from an Fe or Cr atom to an As atom and back to an Fe or Cr atom, the angle by which the electron is deflected as it passes through the As site matters. If this angle is less than 90 degrees, the effective hopping parameter should have one sign, and if the angle is greater than 90 degrees, the effective hopping parameter should have the opposite sign. In a following section, we explore in greater detail the nature of this changing sign.

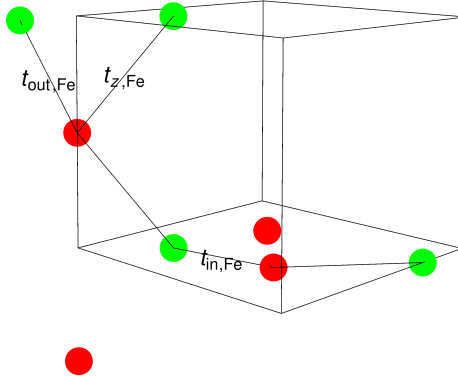


Figure 3.5: Bond types that link a Fe to a neighboring Fe. Green dots represent Fe atoms, while red dots represent As atoms. There are 3 distinct types of hopping connecting a Fe site to a neighboring Fe site.

3.2.3 Derivation of the OOHM

Having used DFT results to motivate writing down the OOHM, we now present a more detailed derivation of the model. We show that we can express a σ -bonding model between the d-electrons and p-electrons in the model, and then we show that the energetics of this type of model, which we call a cluster model, can be fit to the energetics of an effective model.

In order to express a realistic model of FeCrAs, we must have three pieces.

1. We must have information about the microscopic physics.
2. The microscopic information will inform our choice of a basis.
3. The microscopic physics will also give us sufficient information to express a Hamiltonian in this basis.

Microscopic information

The microscopic information that we start with to construct a model of FeCrAs is the crystal structure and chemistry. In Fig. 3.7, we show the crystal structure originally

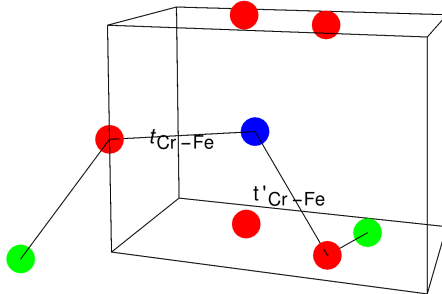


Figure 3.6: Bond types that link a Cr to a neighboring Fe. Green dots represent Fe atoms, blue dots represent Cr atoms, and red dots represent As atoms. There are 2 distinct types of hopping connecting a Cr site to a neighboring Fe site.

shown in chapter 1. The crystal structure and chemistry of FeCrAs will be used later to construct an effective hopping model we call the Optimal Overlap Hopping Model.

Like in chapter 2, we show the electron configurations of Fe, Cr, and As

$$\begin{aligned}
 Fe &: [Ar]4s^23d^6 \\
 Cr &: [Ar]4s^13d^5 \\
 As &: [Ar]4s^23d^{10}4p^3
 \end{aligned} \tag{3.5}$$

We make the same assumption as in chapter 2 that, since As is 3 electrons away from a filled shell, the As sites will absorb 3 electrons, resulting in a 3- charge. In contrast from chapter 2, we assume that the Fe and Cr sites will donate d-electrons to the conduction band, and the relative chemical potentials of these two site types will decide, on average, the number of electrons on each type of site in our model. The orbital types will be used to do the overlap calculation as well as to fit the

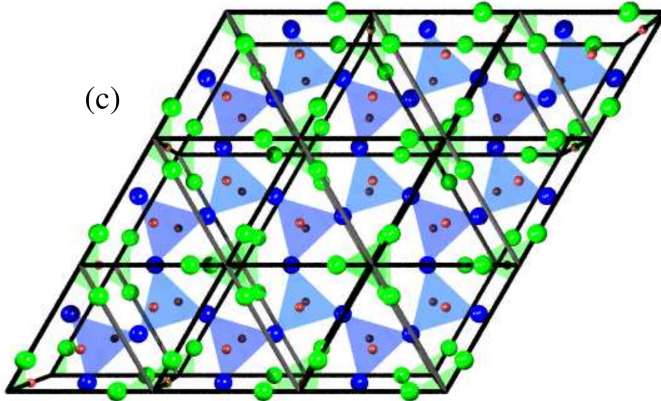


Figure 3.7: Here is a top view of the FeCrAs crystal, taken from Wu et. al. [1]. Cr atoms are shown in blue, Fe atoms are shown in green, and As atoms are shown in red. The blue sites form a distorted kagome lattice.

effective model with the cluster model in the following sections. The crystal field splitting results will be used as a mechanism to move between orbitals, giving rise to a dispersive band structure. Including crystal field splitting terms in the Optimal Overlap Hopping Model is covered near the end of the chapter.

Choosing a basis

We use the orbitals shown in the electron configurations to choose a basis. In particular, we consider a model with p-electrons on the As sites and d-electrons on the Fe and Cr sites. In order to construct the optimal hoppings we mentioned earlier, we consider p-orbitals that point toward the neighboring Cr atoms. To create a p-orbital that points in a certain direction, we simply dot a vector of the Cartesian p-orbitals with a Cartesian vector that points from the As site to the Cr site. Looking at a given Cr site, we see that all of the As atoms in the pyramid that surrounds this Cr site have p-orbitals that point toward said Cr site, as shown in Fig. 3.8.

Using the information about chemistry and the directed p-orbitals we just constructed, we can construct a basis for our effective hopping model. In order to construct the basis, we first calculate the overlap of these directed p-orbitals with the

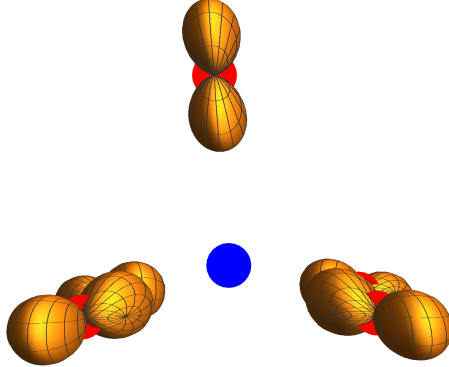


Figure 3.8: We are writing a model with p-orbitals on As sites sigma-bonded to d-orbitals on neighboring Cr and Fe sites, therefore we direct the p-orbitals toward neighboring sites by taking a dot product of the vector that points from a d-electron site to a neighboring As site with the vector of p-orbitals, $\{p_x, p_y, p_z\}$, on said As site. Calculating this dot product for all As neighbors of a Cr gives the directed p-orbitals shown here.

Cartesian d-orbitals. We construct a matrix with elements given by

$$\mathcal{O}_{ij} = \int d^3r \, d_j'(\vec{r}) (\vec{R}_i \cdot \vec{p} (\vec{r} - \vec{R}_i)) \quad (3.6)$$

where $p(\vec{r}) = \{p_x(\vec{r}), p_y(\vec{r}), p_z(\vec{r})\}$ are the Cartesian p-orbitals, $d_j' = \{d_{xy}, d_{xz}, d_{yz}, d_{3z^2-r^2}, d_{x^2-y^2}\}$ are the Cartesian d-orbitals, and \vec{R}_i is the position vector of the vertices of the coordinating polyhedra, indexed by i. In the Cr case, there are 5 As atoms in the coordinating polyhedron, each with a p-electron on them, and 1 Cr atom with 5 d-electrons. Each of the p-orbitals that are on the As sites point toward the Cr site. This forms a 5x5 matrix, where the p-orbitals are the rows and the d-orbitals are the columns.

We use Monte Carlo to find d-orbitals that are optimized to point towards the

directed p-orbitals located on neighboring As atoms. After the overlap calculation, we have an overlap matrix. We are able to find a set of linear combinations of d-orbitals where each linear combination has a strong overlap with only one of the p-orbitals. In other words, we find a transformation that leaves the overlap matrix with large on-diagonal components and small off-diagonal components.

We opted to code a Monte Carlo algorithm because it was possible to find the optimal orbitals this way, and we were able to do it very quickly. This is a small problem that can be solved in more than one way, so our priority was to find a solution quickly.

We choose two columns, or vectors, of the overlap matrix at random, and we rotate them into one another. We call the first vector chosen v_1 , and we call the second one chosen v_2 . The angle through which these vectors rotate we call θ . The new vectors, v'_1 and v'_2 , are

$$\begin{aligned} v'_1 &= \cos(\theta)v_1 - \sin(\theta)v_2 \\ v'_2 &= \sin(\theta)v_1 + \cos(\theta)v_2 \end{aligned} \tag{3.7}$$

We calculate the “energy” of the vectors in the algorithm. This “energy” of a vector is lowest when the on-diagonal component in the overlap matrix is large and the off-diagonal components are small. This is captured in this statement

$$E_v = -|v_d|^2 + \sum_o |v_o|^2 \tag{3.8}$$

where d denotes the on-diagonal component of this vector in the matrix, and o denotes the off-diagonal components of the vector. At the end of each step, we calculate the change in the energy during that step. If the energy is lowered, the

change that was made is kept.

$$\Delta E = E_{v'_1} + E_{v'_2} - E_{v_1} - E_{v_2} \quad (3.9)$$

In other words, if ΔE is negative, we store the changes, and we move to the next iteration. If ΔE is positive, we reject the changes and move to the next iteration. In the n^{th} iteration, if, for example, the two vectors that are randomly chosen are 2 and 4 (representing the 2^{nd} and 4^{th} d-orbitals), the unitary matrix that will perform the rotation in Eq. (3.7) is

$$\mathcal{U}_n = \begin{pmatrix} 1 & 0 & 0 & 0 & 0 \\ 0 & \cos(\theta) & 0 & -\sin(\theta) & 0 \\ 0 & 0 & 1 & 0 & 0 \\ 0 & \sin(\theta) & 0 & \cos(\theta) & 0 \\ 0 & 0 & 0 & 0 & 1 \end{pmatrix}, \quad (3.10)$$

For every iteration that lowers the energy, we store the unitary matrix. The product of all of the saved matrices gives a total unitary transformation matrix

$$\mathcal{U}_{tot} = \mathcal{U}_1 \mathcal{U}_2 \mathcal{U}_3 \dots \mathcal{U}_{N_{acc}}, \quad (3.11)$$

where N_{acc} is the number of times we have accepted changes in the Monte Carlo algorithm. After we have constructed \mathcal{U}_{tot} , we find the optimal overlap orbitals by taking a product of \mathcal{U}_{tot} with the Cartesian orbitals, given by

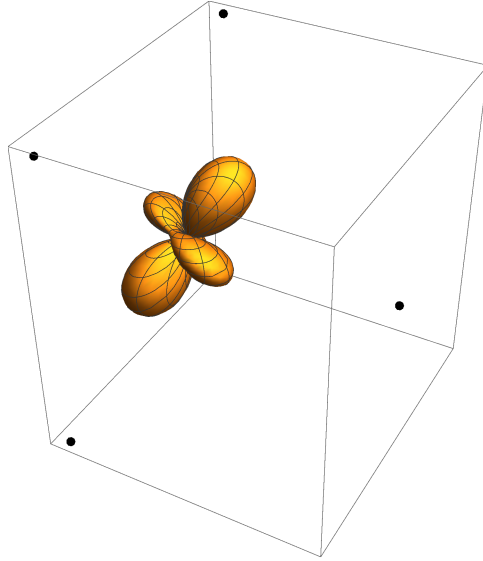


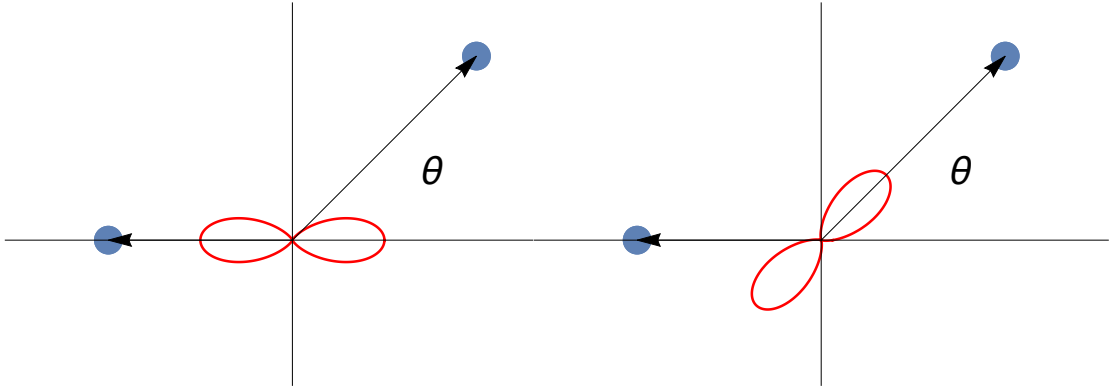
Figure 3.9: Example of an optimal overlap orbital that results from running Monte Carlo. It is a linear combination of d-orbitals that optimizes the overlap with a directed p-orbital on a neighboring As site. There are 5 such orbitals on the Cr sites, as it is surrounded by a pyramid of As atoms.

$$d = \mathcal{U}_{tot} d', \quad (3.12)$$

where d' denotes the set of Cartesian d-orbitals, and d denotes the optimal overlap orbitals, and we show one such orbital in Fig. 3.9.

We run Monte Carlo until the overlap matrix is very nearly diagonal, and then we discard the off-diagonal components. Typically, the off-diagonal components are about a factor of 100 smaller than the on-diagonal components, so it is not unreasonable to discard them. Here, the diagonal matrix represents a model that is exclusively a σ -bonding model between the d-orbitals and the p-orbitals. The electrons in the σ -bonding model, though, are localized in real space, which gives all flat bands in k space. In order to give dispersion to the bands, we later add onsite crystal field splitting terms as a mechanism to move between orbitals on a given site.

In appendix B, we also obtain flat bands as a result of electrons that are localized



(a) p-orbital that points toward the Cr (b) p-orbital that points toward the Cr
on the left on the left

Figure 3.10: p-orbitals on an As atom that is the nearest neighbor to two Cr atoms. We use these figures to construct the cluster model, Eq. (3.14).

in real space. In both the silicon case and the OOHM case, we add onsite terms that move the electrons from one orbital to another on a given site.

Cluster model and hopping processes

In this section, we study a cluster model for the Cr-As-Cr hopping processes in Fe-CrAs and then we consider an effective model. We calculate the energies of these models to show that, if we include a hopping parameter in the effective model that is proportional to $\cos(\theta)$, the cluster and effective models fit with one another. Here, we start with the specific example of a Cr-As-Cr cluster and we use the same reasoning for any A-As-B cluster, where A = Fe, Cr and B = Fe, Cr. Shown here is a figure of the arrangement of the d-electron sites and the p-orbitals the reside on the As site that mediates the conduction of an electron between the first Cr site, and the second Cr site.

The total number of electrons here is conserved. As a result, we have the freedom to set one of the chemical potentials equal to zero. So we choose Δ_p to be zero. Given this simplifying assumption, we have the cluster model

$$H_{Cr-As-Cr} = -t_1 d_1'^\dagger (\vec{p} \cdot \vec{r}_1) - t_2 d_2'^\dagger (\vec{p} \cdot \vec{r}_2) + h.c. + \Delta_{d'_1} d_1'^\dagger d_1' + \Delta_{d'_2} d_2'^\dagger d_2' \quad (3.13)$$

We then further simplify the Hamiltonian by looking at the picture we have drawn to describe the hopping process in the cluster model. We calculate the dot products and express the Hamiltonian in the (d'_1, d'_2, p_x, p_y) basis, giving

$$H_{Cr-As-Cr} = \begin{pmatrix} \Delta_{d'_1} & 0 & r_1 t_1 & 0 \\ 0 & \Delta_{d'_2} & -r_2 t_2 \cos(\theta) & -r_2 t_2 \sin(\theta) \\ r_1 t_1 & -r_2 t_2 \cos(\theta) & 0 & 0 \\ 0 & -r_2 t_2 \sin(\theta) & 0 & 0 \end{pmatrix} \quad (3.14)$$

Next we consider an effective model with a hopping parameter that is proportional to $\cos(\theta)$, as we mentioned earlier. The effective model is

$$H_{Cr-Cr} = t \cos(\theta) d_1^\dagger d_2 + h.c. + \Delta_{d_1} d_1^\dagger d_1 + \Delta_{d_2} d_2^\dagger d_2 \quad (3.15)$$

Written in the (d_1, d_2) basis, this model is

$$H_{Cr-Cr} = \begin{pmatrix} \Delta_{d_1} & t \cos(\theta) \\ t \cos(\theta) & \Delta_{d_2} \end{pmatrix} \quad (3.16)$$

Fig. 3.11 shows both the cluster model and the effective model. The curves from the two models only differ by as much as about 10^{-5} , thus they look like they are the same curve to the eye.

The parameters that have been chosen for the cluster model are

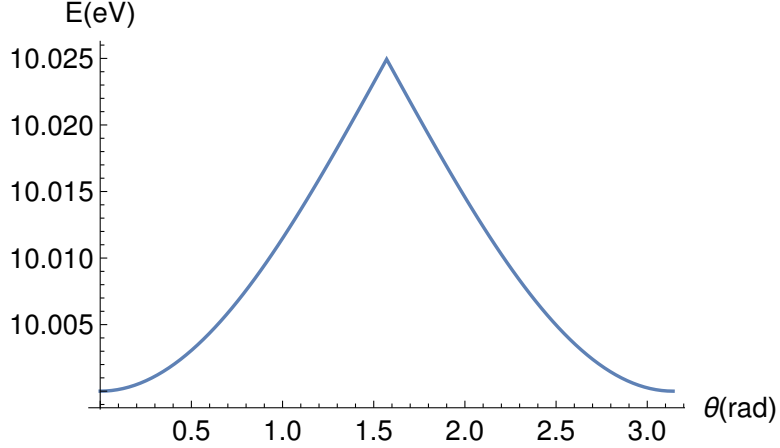


Figure 3.11: Plot of Cluster Model and Effective Model eigenvalues vs bond angle (θ). We show that for the right choice of parameters, the effective model fits the cluster model. This gives us some justification for the $\cos(\theta)$ factor that enters the effective hopping term.

$$t_1 = .5eV$$

$$t_2 = .5eV \quad (3.17)$$

$$\Delta_{d_1} = 10eV$$

$$\Delta_{d_2} = 10eV$$

and those chosen for the effective model are

$$t' = .025eV$$

$$\Delta'_{d_1} = 10.025eV \quad (3.18)$$

$$\Delta'_{d_2} = 10.025eV$$

The effective model that we consider has an effective hopping parameter $t_{eff} = t \cos(\theta)$. Fitting the cluster model with the effective model in this section shows that modeling this hopping parameter with a $\cos(\theta)$ dependence gives us a model that

accurately captures the numerics of the cluster model. This result is like Emery's result from 1987, where he found that the sign of the hopping depended on the bond angle [68].

Crystal field splitting

As was mentioned in chapter 1, the Cr atoms are coordinated, or surrounded, by a pyramid of As atoms. Similarly, Fe atoms are coordinated by a tetrahedron of As atoms.

In order to get a dispersive band structure that we compare to DFT calculations, we need a mechanism to move between orbitals on a given site. Crystal field splitting is one such mechanism. We show the types of terms that we will have after we are done with our crystal field splitting calculation

$$H''_{CF} = \sum_{i\alpha} \epsilon_\alpha d''_{i\alpha}^\dagger d''_{i\alpha} \quad (3.19)$$

$$H_{CF} = \sum_{i\alpha} X_{\alpha\beta} d_{i\alpha}^\dagger d_{i\beta} \quad (3.20)$$

After diagonalizing the crystal field Hamiltonian, we define a unitary matrix that changes basis from the original Cartesian wavefunctions to the eigenbasis of the crystal field Hamiltonian.

$$\mathcal{U}_{ij}'' = \langle d_i'' | d_j' \rangle \quad (3.21)$$

In addition to this, we construct a unitary matrix resulting from the changes made

in the Monte Carlo calculation

$$\mathcal{U}_{ij} = \langle d_i | d'_j \rangle \quad (3.22)$$

We take the diagonal form of the crystal field Hamiltonian, Eq. (3.19), and we transform it into the Monte Carlo basis using the previously defined \mathcal{U} and \mathcal{U}'' . We express this as

$$H_{CF} = (\mathcal{U}^* \mathcal{U}'')^\dagger H''_{CF} (\mathcal{U}'' \mathcal{U}^T) \quad (3.23)$$

Now that we have written the crystal field splitting term in the optimal overlap basis, we add this crystal field splitting term to the effective hopping model that we wrote. Provided there is an appreciable difference between the eigenvalues of the crystal field Hamiltonian, transforming the Hamiltonian in this way makes the off-diagonal components appreciable. This is our mechanism to move between orbitals on a Cr site. Given that we have this mechanism now, we add this into the Hamiltonian that gave flat bands, and the flat bands become dispersive.

We then consider all three Cr atoms in the unit cell. We find all Cr atoms that are one Cr-As-Cr hopping process away. We also found the aforementioned deflection angle for each one of these processes. This deflection angle enters the effective hopping parameter for each of these processes. We enumerated all of these processes and then constructed the Optimal Overlap Hopping Model. We show the band structure of the Optimal Overlap Hopping Model in Fig. 3.12, with the hopping parameters set to 1, with the exception of $t_{A,Cr}$, which has been set to 6.

In this chapter, we presented all known DFT results for FeCrAs, and we used the DFT results to motivate the construction of an effective hopping model we called the

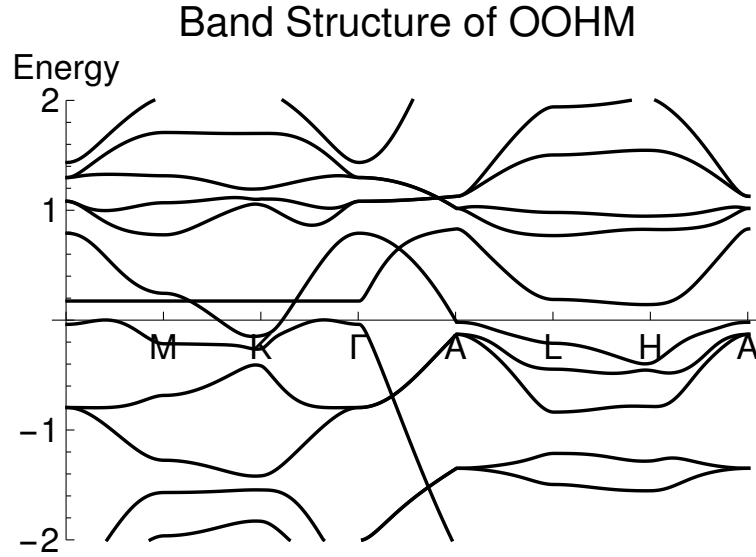


Figure 3.12: Band Structure of Optimal Overlap Hopping Model. We choose all hopping parameters to be 1 eV except for t_{A,C_r} , which we set to 6 eV. We choose these parameters to attempt to fit features of the LDA calculation. The band structure is plotted along the Γ -M-K- Γ -A-L-H-A path.

Optimal Overlap Hopping Model(OOHM). We then expressed a general form of the OOHM. We then expressed a more explicit form of the model. Finally, we presented a derivation of the OOHM by considering microscopic information, constructing a basis via Monte Carlo, and numerically obtaining effective hopping parameters.

Chapter 4

Beyond the Optimal Overlap Hopping Model

In this chapter, we add an interacting term to the Optimal Overlap Hopping Model as an example of how the Optimal Overlap Hopping Model can be used to study FeCrAs, and we gain a preliminary understanding of the magnetism in FeCrAs. We start by considering a magnetic onsite term, and then we proceed to mean-field decouple this term. We consider a ferromagnetic and a $q=0$ coplanar antiferromagnetic case, and we solve the ferromagnetic case self-consistently. We present the resulting self-consistent mean-field parameter result, which is a prediction for the magnetic structure resulting from the OOHM when the spins are fixed in a ferromagnetic state. The non-self-consistent $q=0$ case is then used to calculate a dynamic spin structure factor.

4.1 Onsite Mean Field Theory

Before we add in interactions, we have the OOHM, Eq. 3.1. We seek a greater understanding of the magnetic structure of FeCrAs from within the OOHM, so we consider the onsite magnetic term

$$H_{onsite} = -\frac{J_H^{Cr}}{2} \sum_i (S_i^{Cr})^2 - \frac{J_H^{Fe}}{2} \sum_j (S_j^{Fe})^2 \quad (4.1)$$

where $S_i^{Cr} = \sum_a c_{ia\sigma}^\dagger \tau_{\sigma\sigma'} c_{ia\sigma'}$ and $S_j^{Fe} = \sum_a c_{ja\sigma}^\dagger \tau_{\sigma\sigma'} c_{ja\sigma'}$. J_H^{Cr} denotes a Hund exchange coupling for the Cr sites, while J_H^{Fe} denotes a Hund exchange coupling for the Fe sites. We then mean-field decouple Eq. (4.1) in S, which gives

$$H_{onsite,MF} = -J_H^{Cr} \sum_i \langle S \rangle_i^{Cr} \cdot \left(S_i^{Cr} - \frac{\langle S \rangle_i^{Cr}}{2} \right) - J_H^{Fe} \sum_j \langle S \rangle_j^{Fe} \cdot \left(S_j^{Fe} - \frac{\langle S \rangle_j^{Fe}}{2} \right) \quad (4.2)$$

with

$$\vec{S}_{Cr} = \sum_{k,a \in Cr} \frac{1}{2N_{Cr}} M_{a\sigma,\alpha}^* \vec{\tau}_{\sigma\sigma'} M_{a\sigma',\alpha} \quad (4.3)$$

and

$$\vec{S}_{Fe} = \sum_{k,a \in Fe} \frac{1}{2N_{Fe}} M_{a\sigma,\alpha}^* \vec{\tau}_{\sigma\sigma'} M_{a\sigma',\alpha} \quad (4.4)$$

where M is the matrix of eigenvectors. In M , each eigenvector forms a column.

4.1.1 Ferromagnetic Case

Here, we calculate the ferromagnetic case self-consistently. This is the case where the spin mean-field parameters all point in the same direction but do not have fixed length. Thus, we have only the z mean-field parameters

$$\begin{aligned}
S_{Cr}^z &= \frac{1}{2N_{Cr}} \sum_{k,a \in Cr} \langle gnd | c_{k,a,\uparrow}^\dagger c_{k,a,\uparrow} - c_{k,a,\downarrow}^\dagger c_{k,a,\downarrow} | gnd \rangle \\
&= \frac{1}{2N_{Cr}} \sum_{k,a \in Cr} [M_{a\uparrow,\alpha}^* M_{a\uparrow,\beta} \langle gnd | \gamma_\alpha^\dagger \gamma_\beta | gnd \rangle - M_{a\downarrow,\alpha}^* M_{a\downarrow,\beta} \langle gnd | \gamma_\alpha^\dagger \gamma_\beta | gnd \rangle] \quad (4.5) \\
&= \frac{1}{2N_{Cr}} \sum_{k,a \in Cr, E_\alpha < 0} [M_{a\uparrow,\alpha}^* M_{a\uparrow,\alpha} - M_{a\downarrow,\alpha}^* M_{a\downarrow,\alpha}]
\end{aligned}$$

We also define chemical potentials for the Cr and Fe sites as

$$\begin{aligned}
\mu^{Cr} &= \mu + \delta \\
\mu^{Fe} &= \mu - \delta
\end{aligned} \quad (4.6)$$

Additionally, we define spin-up and spin-down chemical potentials

$$\begin{aligned}
\mu_\uparrow^{Cr} &= \mu^{Cr} + J_H^{Cr} S_z^{Cr} \\
\mu_\downarrow^{Cr} &= \mu^{Cr} - J_H^{Cr} S_z^{Cr} \\
\mu_\uparrow^{Fe} &= \mu^{Fe} + J_H^{Fe} S_z^{Fe} \\
\mu_\downarrow^{Fe} &= \mu^{Fe} - J_H^{Fe} S_z^{Fe}
\end{aligned} \quad (4.7)$$

These chemical potentials are defined by noting that they are simply the coefficient of the number operator. In our calculations, we set $\delta = .5eV$. The chemical potentials are chosen so that the total number of electrons in the unit cell is 33, which is the total number of electrons in the valence, provided the As sites have a charge of 3-. Running the self-consistent mean field theory, our plots for the spin mean-fields for Cr and Fe converge, shown in Fig. 4.1. We see quite readily is that S_z^{Cr} converges to nearly 0, while S_z^{Fe} converges to a much larger number. A prediction of our model emerges in this plot; when the spins are fixed ferromagnetically, Fe dominates the

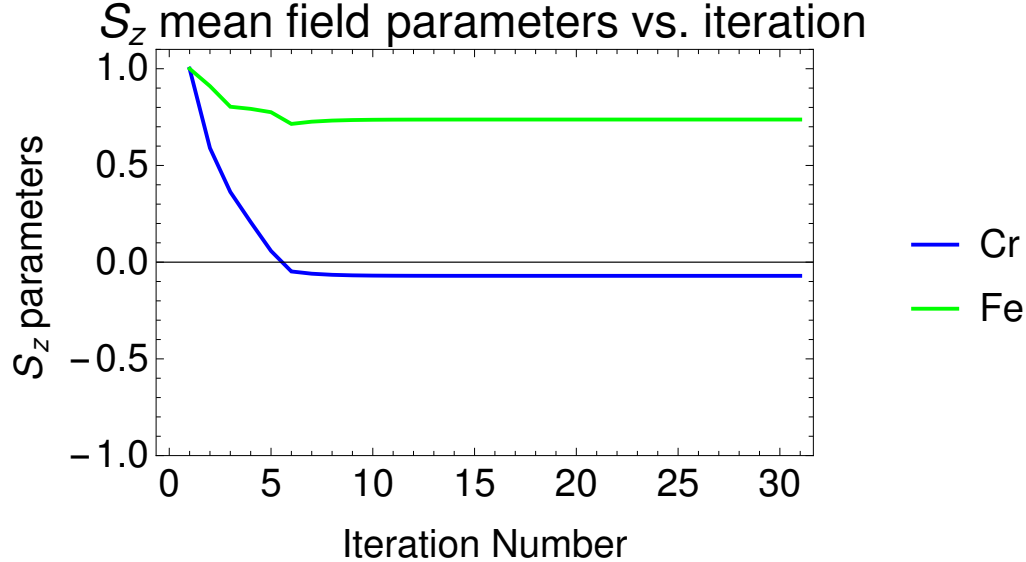


Figure 4.1: Results from the self-consistent mean field theory calculation, using the ferromagnetic case of the Hamiltonian in Eq. (4.10). Spin mean fields are shown for Cr(Blue) and Fe(Green) vs. iteration. It is interesting that Cr converges to a very small spin moment, while Fe stays quite large. Perhaps we can ascribe the dominance of the Fe spin mean field to the fact that we have chosen a ferromagnetic state, and Fe often tends to be ferromagnetic.

magnetism.

4.1.2 Q=0 case

Taking a step toward the $\sqrt{3} \times \sqrt{3}$, we next take a look at the q=0. The q=0 state is one where three spins, \vec{S}_A , \vec{S}_B , and \vec{S}_C all point toward the center of the triangle on which they reside. This pattern of spins is repeated in all unit cells.

Noting that for a q=0 magnetic state $\langle S \rangle_{Rd} = \langle S \rangle_d$, we have

$$\begin{aligned}
H_{onsite,MF} = & - J_H^{Cr} \sum_{Rd} \langle S \rangle_d^{Cr} \cdot \left(S_{Rd}^{Cr} - \frac{\langle S \rangle_d^{Cr}}{2} \right) \\
& - J_H^{Fe} \sum_{R'd'} \langle S \rangle_{d'}^{Fe} \cdot \left(S_{R'd'}^{Fe} - \frac{\langle S \rangle_{d'}^{Fe}}{2} \right)
\end{aligned} \tag{4.8}$$

Substituting in the Abrikosov fermion form [69] for the quantum spins and Fourier transforming we have

$$\begin{aligned}
H_{onsite,MF} = & - \frac{J_H^{Cr}}{N_u} \sum_d \langle S \rangle_d^{Cr} \cdot \left(\sum_R \left(\sum_k \tilde{c}_{kda\sigma}^{Cr\dagger} e^{-i\vec{k} \cdot \vec{R}} \right) \vec{\tau}_{\sigma\sigma'} \left(\sum_{k'} \tilde{c}_{k'da\sigma'}^{Cr} e^{i\vec{k}' \cdot \vec{R}} \right) \right) \\
& - \frac{J_H^{Fe}}{N_u} \sum_{d'} \langle S \rangle_{d'}^{Fe} \cdot \left(\sum_{R'} \left(\sum_k \tilde{c}_{kd'a\sigma}^{Fe\dagger} e^{-i\vec{k} \cdot \vec{R}'} \right) \vec{\tau}_{\sigma\sigma'} \left(\sum_{k'} \tilde{c}_{k'd'a\sigma'}^{Fe} e^{i\vec{k}' \cdot \vec{R}'} \right) \right) \\
& + C
\end{aligned} \tag{4.9}$$

The Fourier transform gives a condition on the momenta that leaves the Hamiltonian diagonal in k-space. The Fourier transform of the onsite mean-field model is

$$\begin{aligned}
H_{onsite,MF} = & - J_H^{Cr} \sum_d \langle S \rangle_d^{Cr} \cdot \left(\sum_k \tilde{c}_{kda\sigma}^{Cr\dagger} \vec{\tau}_{\sigma\sigma'} \tilde{c}_{kda\sigma'}^{Cr} \right) \\
& - J_H^{Fe} \sum_{d'} \langle S \rangle_{d'}^{Fe} \cdot \left(\sum_k \tilde{c}_{kd'a\sigma}^{Fe\dagger} \vec{\tau}_{\sigma\sigma'} \tilde{c}_{kd'a\sigma'}^{Fe} \right) + C
\end{aligned} \tag{4.10}$$

We use Eq. (4.10) for the mean field theory of the $q=0$ state later in the present chapter, when we calculate a dynamic spin structure factor.

4.2 Neutron Scattering and Dynamic Spin Structure Factor

The starting point for our calculation of a dynamic spin structure factor is ¹

¹Young-June Kim, from the University of Toronto, has measured the inelastic neutron scattering from powder samples of FeCrAs. The data has not yet been published, so we do not show the data in the present thesis.

$$S(\vec{q}, \omega) = \frac{1}{N_s} \sum_{ij} \int dt \langle \vec{S}_i(0) \cdot \vec{S}_j(t) \rangle e^{-i\vec{q} \cdot (\vec{r}_i - \vec{r}_j)} e^{i\omega t} \quad (4.11)$$

We express each of the spins in their Abrikosov Fermion form [69] given by

$$\vec{S}_i = \frac{1}{2} \sum_{\alpha} c_{i\alpha\sigma}^{\dagger} \vec{\tau}_{\sigma\sigma'} c_{i\alpha\sigma'} \quad (4.12)$$

$$= \frac{1}{2} \sum_{\alpha} c_{Rd\alpha\sigma}^{\dagger} \vec{\tau}_{\sigma\sigma'} c_{Rd\alpha\sigma'} \quad (4.13)$$

where here, \vec{R} denotes a Bravais lattice vector, \vec{d} denotes a sublattice vector, α is a d orbital label, and $\vec{\tau}$ is the vector of Pauli matrices.

The calculation of the dynamic spin structure factor is complicated. Therefore, we have placed these details in Appendix C. The final result we arrive at for the dynamic spin structure factor in the appendix is

$$S(\vec{q}, \omega) = \frac{1}{4N_s} \sum_{dd'} \sum_{\alpha\alpha'} \sum_{\sigma\sigma'\sigma''\sigma'''} \sum_{kk'} \sum_G \sum_{\lambda \in E_{\lambda} < 0, \lambda' \in E_{\lambda'} > 0} (2f(\sigma, \sigma', \sigma', \sigma) - f(\sigma, \sigma, \sigma', \sigma')) \quad (4.14)$$

$$\times \delta(E_{\lambda} - E_{\lambda'} + \omega) e^{i\vec{q} \cdot (\vec{d}' - \vec{d})} \quad (4.15)$$

where

$$f(\sigma, \sigma', \sigma'', \sigma''') = M(k)_{\lambda, d\alpha\sigma}^{\dagger} M(k + q + G)_{d\alpha\sigma', \lambda'} M(k + q + G)_{\lambda', d'\alpha'\sigma''}^{\dagger} M(k)_{d'\alpha'\sigma''', \lambda} \quad (4.16)$$

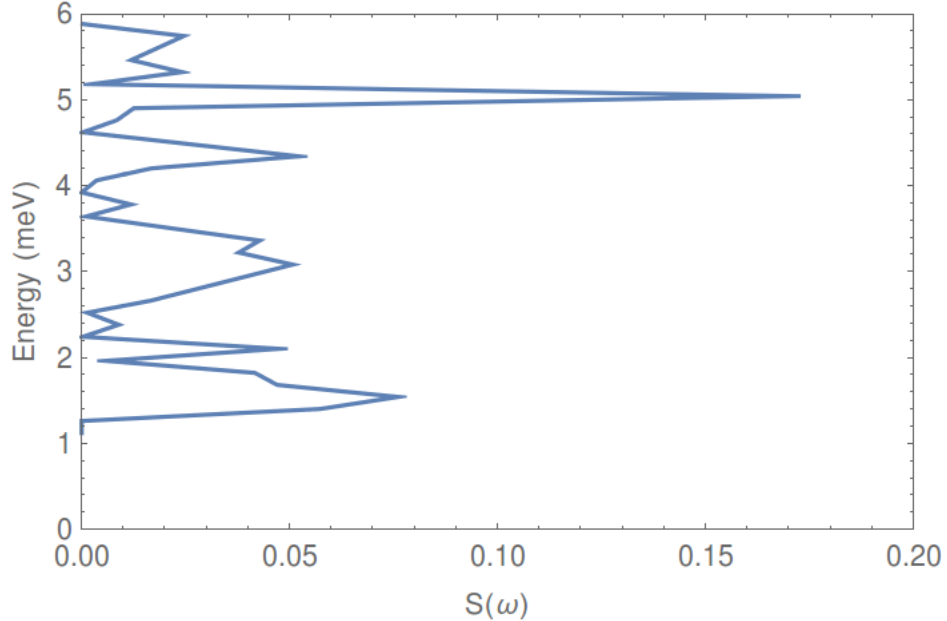


Figure 4.2: Momentum-averaged dynamic spin structure factor, $S(\omega)$, plotted between 0 meV and 6 meV. The independent axis here is the wavenumber in the calculation. For this calculation we calculated the structure factor along the b_1 direction in k space and summed over all k points. The benefit of making such a plot is that we observe that our model features spin excitations down to low energies.

We use Eq. 4.15 to generate all of the contributions to the structure factor assuming the $q=0$ case from the mean-field calculation. To try to match our dynamic spin structure factor calculation with our collaborator, we placed the contributions to the structure factor in bins corresponding to a range in q and ω . We then summed over all momenta to calculate a momentum-averaged dynamic spin structure factor. We show the low energy momentum-averaged dynamic spin structure factor in Fig. 4.2 and the high energy momentum-averaged dynamic spin structure factor in Fig. 4.3.

4.3 Computational Cost

Here we summarize the computational cost of the dynamic spin structure factor calculation for future use. In order to calculate the dynamic spin structure factor, we must have all eigenvalues and eigenvectors for the OOHM at every point in k

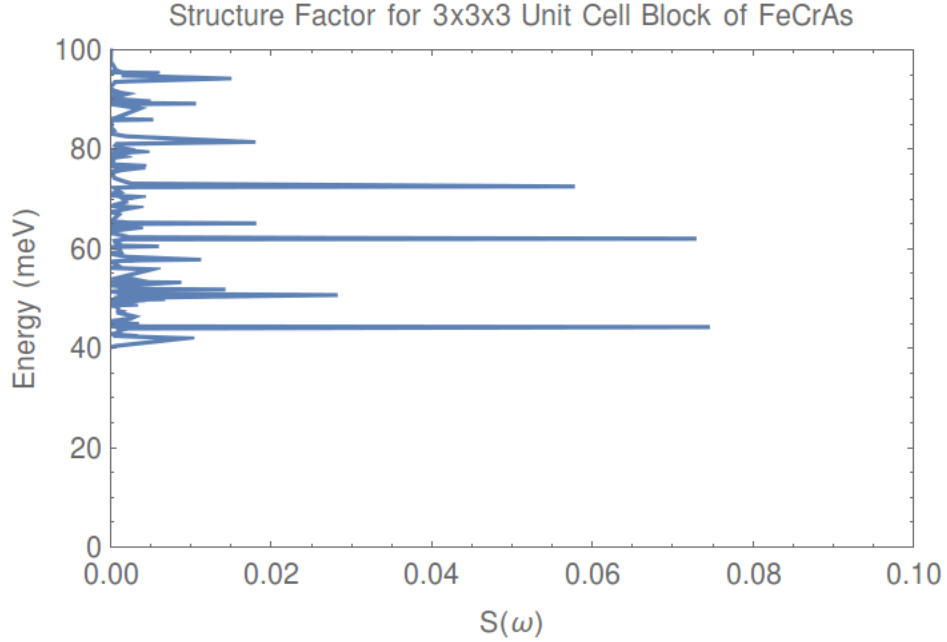


Figure 4.3: Momentum-averaged dynamic spin structure factor, $S(\omega)$, plotted between 40 meV and 100 meV. The independent axis here is the wavenumber in the calculation. For this calculation we calculated the structure factor along the b_1 direction in k space and summed over all k points.

space. Since we were considering a 3-dimensional system, the number of k points scales as N_{sites} . The time required to find eigensystems became prohibitive at about $6unitcell \times 6unitcell \times 6unitcell$ system size, with a fixed Hamiltonian size of 180×180 for the $q=0$ state. After calculating these Hamiltonians and eigensystems, we use the eigensystems to calculate the dynamic spin structure factor, which is the product of many different combinations of 4 matrix element products. The computational cost of the dynamic spin structure factor is a result of the combinations of sites, orbitals, spins, and eigenlabels. Looking at Eq. 4.16, we estimate the number of terms in the dynamic spin structure factor as $(6 \text{ sites})^2 \times (5 \text{ d-orbitals})^2 \times (2 \text{ spin values})^2 \times 33 \text{ filled energy levels} \times 27 \text{ unfilled energy levels} \times N_{sites} \approx 3,000,000N_{sites}$.

Chapter 5

Conclusion

Here, we present a summary of results in the present thesis, and then we discuss the implications of the results. Subsequently, we discuss how our models can be used to study FeCrAs.

5.1 Summary of results

In chapter 1, we presented experimental data for FeCrAs from Wu et. al. [1]. In particular, we showed the resistivity, heat capacity, and magnetic susceptibility of single-crystal samples of FeCrAs. The experimental data shows that FeCrAs is a rare material that is neither a metal nor an insulator, and it has yet to be explained. We illustrated how our theories complement existing theories for FeCrAs using the metallicity spectrum.

In chapter 2, we motivated the study of the Kondo Lattice Model on the kagome lattice. We then proceeded to study the model numerically, and we found the phase diagram of the model. We found a host of complex spin orders, in addition to some spin orders that were more well-known. One of these spin orders, the $\sqrt{3} \times \sqrt{3}$ state, is the state that is experimentally observed in FeCrAs.

In chapter 3, we presented DFT (LDA, LDA+U, and GGA) results for FeCrAs.

All of these results had the feature that the d-orbital density of states near the Fermi energy was high, while the p-orbital density of states near the Fermi energy was low. Consequently, we constructed an effective hopping model, called the Optimal Overlap Hopping Model, consisting only of d-orbitals for FeCrAs. The Optimal Overlap Hopping Model serves as our second starting point for further calculations.

In chapter 4, we added a magnetic mean-field term to the Optimal Overlap Hopping Model. By adding interactions to the Optimal Overlap Hopping Model, we showed how the Optimal Overlap Hopping Model can be used to study FeCrAs. We also presented

5.2 Discussion

We presented two separate starting points for the study of FeCrAs. The first starting point we presented was the kagome Kondo Lattice Model, which could be used to understand qualitative features of FeCrAs. The second starting point we presented was the Optimal Overlap Hopping Model, which could be used to understand quantitative features of FeCrAs. By adding interactions to the Optimal Overlap Hopping Model, we may be able to explain the experimental data.

If our aim is to describe the resistivity, the Kondo Lattice Model is likely the appropriate starting point from which we can launch a study. We believe that if an electron is to hop around on the kagome lattice, its momentum will be relaxed if these classical moments are fluctuating due to non-zero temperature. The resistivity that would result would be larger than that of a metal, which would potentially give the desired “bad metal” behavior.

If one was concerned with the mutilation of the Fermi surface, the Optimal Overlap Hopping Model from chapter 3 would likely be the appropriate starting point. Given that we have knowledge of all of the orbitals of interest, and we have control over

all hopping parameters, we could conceivably develop an understanding of the Fermi surface. We could then construct a quantum field theory for the Fermi surface, and we would investigate whether the Fermi surface is robust to the addition of interactions. Another property we could study with the Optimal Overlap Hopping Model is the band structure. If one were to measure the band structure with ARPES, we could adjust the parameters of the Optimal Overlap Hopping Model to attempt to fit the ARPES band structure.

If one wanted to study the magnetism with the Optimal Overlap Hopping Model, interactions can be added to the Optimal Overlap Hopping Model. Given that there are local moments on the Cr sites in FeCrAs, one must include additional considerations in our Optimal Overlap Hopping Model. In chapter 4, we added the mean-field decoupled interaction terms to the Optimal Overlap Hopping Model. In the dynamic spin structure factor, we only have particle-hole spin excitations. Our model does not have spin wave physics. It seems that we cannot simply add interactions at the mean-field level if we are to see local moment physics in our results. We need to go beyond these simple mean-field considerations. A potential direction one could pursue is Random Phase Approximation (RPA).

Appendix A

Hamiltonian and band structure of nearest neighbor kagome lattice : review

A.1 Writing a Hamiltonian

We present a brief review of calculating the band structure of a tight-binding model. This will hopefully prepare an otherwise unprepared reader to calculate the band structures of such models, in preparation for chapter 3. We discuss a single-orbital hopping model on the kagome lattice. We are motivated to choose this lattice to study because Cr atoms lie on a distorted version of the kagome lattice, and Cr atoms dominate the magnetism in FeCrAs. We express the model, Fourier transform it to put it in a soluble form, and plot the energy band structure of this model.

The kagome lattice has the same primitive vectors as the hexagonal and triangular lattices, but it has a basis of three sites. We see these 3 site types repeated several times in Fig. A.1. The angle between the a_1 and a_2 vectors is 120° .

We use second quantized notation to express tight-binding models [70]. Second

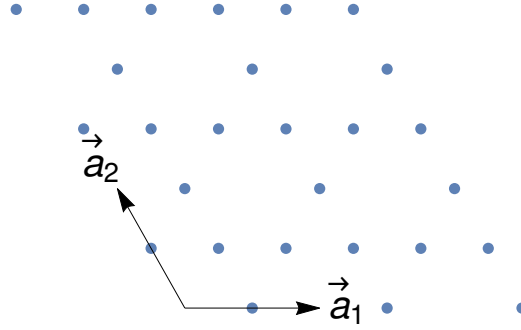


Figure A.1: The kagome lattice is a triangular lattice with a basis. Along with lattices such as the triangular lattice and the pyrochlore lattice, it has been one of the central foci of the field of frustrated magnetism. The primitive vectors are $\vec{a}_1 = a\{1, 0\}$ and $\vec{a}_2 = a\{-\frac{1}{2}, \frac{\sqrt{3}}{2}\}$. The basis vectors are $\frac{1}{2}\vec{a}_1$, $\frac{1}{2}\vec{a}_2$, and $\frac{1}{2}(\vec{a}_1 + \vec{a}_2)$.

quantized notation is used to create and destroy particles on lattices that we are interested in. We choose second quantized notation because we can usually solve the models readily in this notation. Given a lattice, the sites of which are indexed by i , we represent the annihilation (or destruction) of an electron on this site with spin σ by $c_{i\sigma}$ ($c_{i\sigma}^\dagger$). Using these operators, we can express a model for electrons that can hop from any of the sites to any of their neighbors

$$H_{hop} = -t \sum_{\langle ij \rangle \sigma} c_{i\sigma}^\dagger c_{j\sigma} + h.c. \quad (\text{A.1})$$

Here, t is what is known as the tunneling, or hopping, energy and c_i^\dagger creates a fermion on a site with label i . There is a minus sign in front of the t because this is a model for conduction, and so it is designed to be energetically favorable for the electron to hop. Also, $\langle ij \rangle$ means that i and j are nearest neighbors of one another, and $h.c.$ stands for hermitian conjugate.

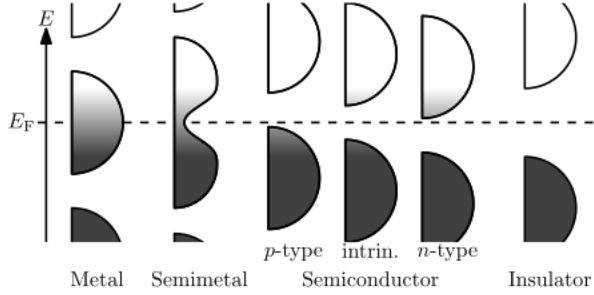


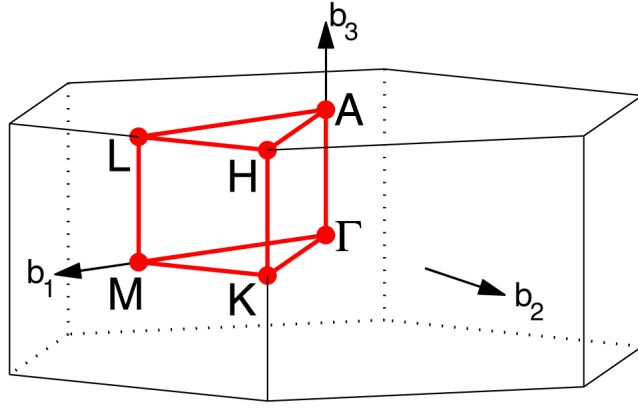
Figure A.2: Pictorial description of the density of states of various basic states of matter [8]

A.2 Calculating a band structure

An energy band structure is a plot of energy vs. momentum. This plot may be calculated, and is directly measurable using angle-resolved photoemission spectroscopy (ARPES). Band structures help us make statements about the properties of a material. When we calculate energy bands, we define the Fermi energy by filling electrons into the energy levels of the spectrum, starting with the lowest energy. The Fermi energy is the energy of the last electron that we place in the energy levels. The Fermi energy is important because the density of states around this energy is essential for understanding how a material will behave. Metals have many bands around the Fermi energy. Electrons in these bands have many options for movement, or conduction. Insulators have a large gap in the density of states around the Fermi energy, so it is difficult to get the electrons to conduct, because a great deal of energy must be used to excite the electrons into other states. Fig. A.2 shows some samples of what the band structures look like for certain types of materials.

From these primitive vectors, shown in Fig. A.1, we find the reciprocal lattice (momentum) vectors. These vectors give us the necessary information to construct the Brillouin Zone. The shape of the hexagonal Brillouin zone with high symmetry points is shown in Fig. A.3.

Once we have decided the path we will take through momentum space, we Fourier



HEX path: $\Gamma\text{-}M\text{-}K\text{-}\Gamma\text{-}A\text{-}L\text{-}H\text{-}A\mid L\text{-}M\text{-}K\text{-}H$

[Setyawan & Curtarolo, DOI: 10.1016/j.commatsci.2010.05.010]

Figure A.3: Brillouin zone of a hexagonal crystal structure with a path in red that is conventionally taken when plotting band structures for hexagonal structures [9]

transform our Hamiltonian and plot all of the energies of our model along this path.

We use the following definition of the Fourier transform

$$c_i = \sum_k c_{k,d_i} e^{i\vec{k} \cdot \vec{R}_i} \quad (\text{A.2})$$

where R_i is a Bravais lattice vector for the site i and d_i is the basis vector that takes on one of three values.

$$H_{hop} = -t \sum_{\langle ij \rangle} \sum_{k,k'} c_{k,d_i}^\dagger c_{k',d_j} e^{-i\vec{k} \cdot \vec{R}_i + i\vec{k}' \cdot \vec{R}_j} + h.c. \quad (\text{A.3})$$

then we use the following identity to make this model diagonal in k-space

$$\sum_{\vec{R}} e^{-i\vec{k} \cdot \vec{R} + i\vec{k}' \cdot \vec{R}} = N_u \delta_{kk'} \quad (\text{A.4})$$

In our mean field theory we do a finite size analysis. When we do finite size analysis we need to think carefully about what type of boundary conditions we will use. Currently we are using Born- von Karman (BVK) boundary conditions [71]. We use BVK boundary conditions because they are conditions that represent an ideal crystal. These boundary conditions impose a periodic restriction on the wavefunction.

This gives for the allowed k points

$$\vec{k} = k_1 \vec{b}_1 + k_2 \vec{b}_2 + k_3 \vec{b}_3 \quad (\text{A.5})$$

where $k_n = \frac{2\pi m_n}{N_n}$ and $m_n = 0, 1, \dots, N_n - 1$ and N_n is the number of unit cells along the \vec{a}_n direction. The total number of units cells in the system is $N_u = N_1 N_2 N_3$, and the number of sites in the lattice is the number of unit cells times the number of sites in the unit cell, which for the kagome lattice is $N_s = 3N_u$.

The k_n take on specific values because of the Born-von Karman boundary conditions. For each of these BVK k points, we construct a Hamiltonian, and consequently we find a spectrum for said Hamiltonian.

Once we have Fourier transformed the hopping model, we plot the band structure for a given path around the Brillouin zone. Shown in Fig. A.4 is the band structure of the nearest neighbor hopping model on the kagome lattice.

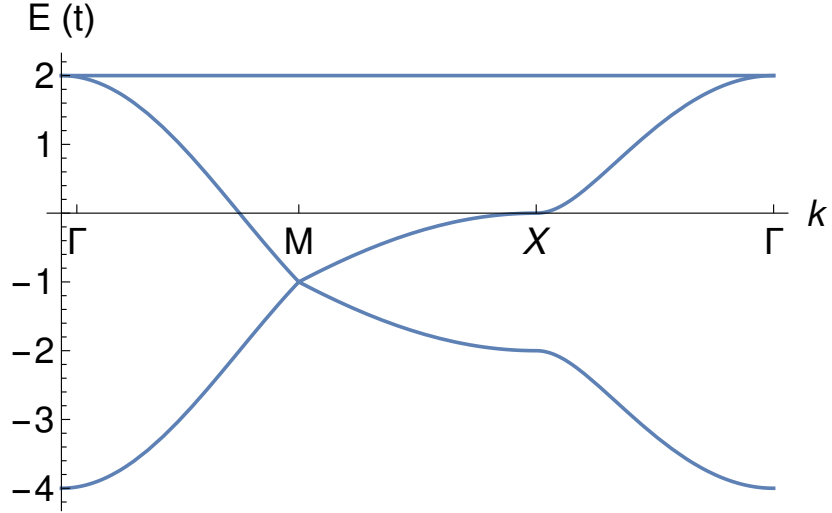


Figure A.4: Band structure of the nearest neighbor hopping model on the kagome lattice. The high-symmetry path taken is Γ - M - X - Γ . The flat band is a signal of the geometric frustration of the kagome lattice. The hopping parameter, t , is set to 1 in this calculation.

$$\tilde{H}_{hop}(\vec{k}) = -2t \begin{pmatrix} 0 & 1 + e^{-ik_2} & 1 + e^{-ik_1} \\ 1 + e^{ik_2} & 0 & 1 + e^{i(-k_1+k_2)} \\ 1 + e^{ik_1} & 1 + e^{i(k_1-k_2)} & 0 \end{pmatrix} \quad (\text{A.6})$$

Appendix B

Silicon hybrid hopping model

In this appendix, we study a hopping model for silicon using the sp^3 hybrid orbitals [11]. Silicon is in the 3p block. This means that the electrons in silicon's outer shell are s and p electrons. We consider a model for one site in the lattice of silicon atoms, given by

$$H_{onsite} = \epsilon_s s_\sigma^\dagger s_\sigma + \epsilon_p \sum_\alpha p_{\alpha,\sigma}^\dagger p_{\alpha,\sigma}, \quad (\text{B.1})$$

where ϵ_s is the energy of an s electron, and ϵ_p is the energy of a p electron.

Silicon atoms reside on a diamond lattice, shown in Fig. B.1. We consider an electron moving around from site to site, thus we construct the following hopping model [24]

$$H_{hop} = -t \left(\sum_{\mu_1} c_{R+d_1, \mu_1}^\dagger c_{R+\mu_1, \mu_1} + \sum_{\mu_2} c_{R+d_2, \mu_2}^\dagger c_{R+\mu_2, \mu_2} \right) + h.c. \quad (\text{B.2})$$

where the nearest neighbors of the $\vec{R} + \vec{d}_1$ atom are

$$\vec{R} + \vec{d}_2, \vec{R} - \vec{a}_1 + \vec{d}_2, \vec{R} - \vec{a}_2 + \vec{d}_2, \vec{R} - \vec{a}_3 + \vec{d}_2$$

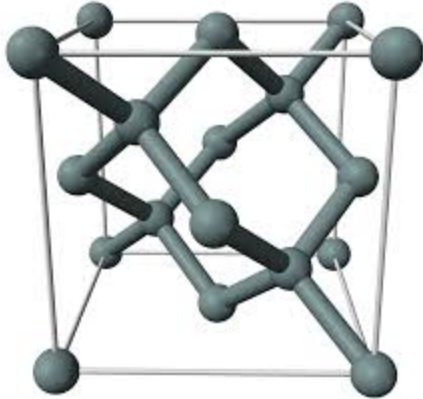


Figure B.1: Diamond lattice of silicon. In the diamond lattice, each site is surrounded by a tetrahedron of neighboring sites [10].

and the orbitals that reside on these atoms are

$$|1\rangle = \frac{1}{2} (|s\rangle + |p_x\rangle + |p_y\rangle + |p_z\rangle) \quad (\text{B.3})$$

$$|2\rangle = \frac{1}{2} (|s\rangle + |p_x\rangle - |p_y\rangle - |p_z\rangle) \quad (\text{B.4})$$

$$|3\rangle = \frac{1}{2} (|s\rangle - |p_x\rangle + |p_y\rangle - |p_z\rangle) \quad (\text{B.5})$$

$$|4\rangle = \frac{1}{2} (|s\rangle - |p_x\rangle - |p_y\rangle + |p_z\rangle). \quad (\text{B.6})$$

The nearest neighbors of the $\vec{R} + \vec{d}_2$ atom are

$$\vec{R} + \vec{d}_1, \vec{R} + \vec{a}_1 + \vec{d}_1, \vec{R} + \vec{a}_2 + \vec{d}_1, \vec{R} + \vec{a}_3 + \vec{d}_1$$

and the orbitals that reside on these atoms are

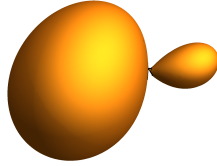


Figure B.2: One of silicon's hybrid orbitals. This is a linear combination of s and p orbitals that results in an orbital that points toward a vertex of a tetrahedron. These orbitals are the 4 (famous) sp^3 hybrid orbitals.

$$|\bar{1}\rangle = \frac{1}{2} (|s\rangle - |p_x\rangle - |p_y\rangle - |p_z\rangle) \quad (\text{B.7})$$

$$|\bar{2}\rangle = \frac{1}{2} (|s\rangle - |p_x\rangle + |p_y\rangle + |p_z\rangle) \quad (\text{B.8})$$

$$|\bar{3}\rangle = \frac{1}{2} (|s\rangle + |p_x\rangle - |p_y\rangle + |p_z\rangle) \quad (\text{B.9})$$

$$|\bar{4}\rangle = \frac{1}{2} (|s\rangle + |p_x\rangle + |p_y\rangle - |p_z\rangle). \quad (\text{B.10})$$

These hybrid orbitals look like those in Fig. B.2. In this hopping model, electrons are restricted. An electron on an atom will only be able to hop to a neighboring site via one of the hybrid orbitals, and when it gets to that neighboring site it will only be able to hop back to the first site. The hybrid basis only allows these kinds of processes. Because the electrons are restricted in this way, this leads to a completely flat band structure. Not only is this uninteresting, it is certainly incorrect. We know that silicon is a semiconductor.

So let's revisit the onsite term

$$H_{onsite} = \begin{pmatrix} \epsilon_s & 0 & 0 & 0 \\ 0 & \epsilon_p & 0 & 0 \\ 0 & 0 & \epsilon_p & 0 \\ 0 & 0 & 0 & \epsilon_p \end{pmatrix} \quad (\text{B.11})$$

We should note a couple things about this matrix. Clearly, this is a diagonal matrix, but because $\epsilon_p \neq \epsilon_s$, it is not a multiple of the identity matrix. This is crucial. When we transform the identity matrix into another basis, it remains the identity matrix. The identity matrix is diagonal in every basis. Transforming this onsite energy matrix into a different basis, though, yields a matrix with non-zero off-diagonal components. Let's choose the hybrid orbital basis that our hopping term is written in. When we transform the onsite term into the hybrid orbital basis, the non-zero off-diagonal elements of the matrix that result represent moving from one hybrid orbital to another on a given site. So, we have solved the previous problem we had. Initially, electrons were stuck moving back and forth between two sites, which led to a flat band structure (an insulator).

$$\tilde{\epsilon} = \begin{pmatrix} \epsilon_p + \frac{\Delta}{4} & \frac{\Delta}{4} & \frac{\Delta}{4} & \frac{\Delta}{4} \\ \frac{\Delta}{4} & \epsilon_p + \frac{\Delta}{4} & \frac{\Delta}{4} & \frac{\Delta}{4} \\ \frac{\Delta}{4} & \frac{\Delta}{4} & \epsilon_p + \frac{\Delta}{4} & \frac{\Delta}{4} \\ \frac{\Delta}{4} & \frac{\Delta}{4} & \frac{\Delta}{4} & \epsilon_p + \frac{\Delta}{4} \end{pmatrix} \quad (\text{B.12})$$

So, after writing the onsite term in the hybrid basis, we express the general form of the total Hamiltonian

$$H_{silicon} = H_{hop} + H_{onsite} \quad (\text{B.13})$$

Fourier transforming this model we have

$$\tilde{H}_{hop} = \sum_k \left[c_{kd_1\mu}^\dagger \epsilon_{\mu\mu'} c_{kd_1\mu'} + c_{kd_2\bar{\mu}}^\dagger \epsilon_{\bar{\mu}\bar{\mu}'} c_{kd_2\bar{\mu}'} \right] \quad (\text{B.14})$$

$$- t \sum_k \left[\sum_{\mu_1} e^{i\vec{k}\cdot\vec{\mu}_1} c_{kd_1\mu_1}^\dagger c_{kd_2\mu_1} - \sum_{\mu_2} e^{i\vec{k}\cdot\vec{\mu}_2} c_{kd_2\mu_2}^\dagger c_{kd_1\mu_2} \right] \quad (\text{B.15})$$

Defining the eight-component vector of fermion operators

$$\psi_k^\dagger = (c_{k,d_1,1}^\dagger, \dots, c_{k,d_1,4}^\dagger, c_{k,d_2,1}^\dagger, \dots, c_{k,d_2,4}^\dagger) \quad (\text{B.16})$$

we express the Hamiltonian in the form

$$H = \sum_k \psi_k^\dagger h_k \psi_k \quad (\text{B.17})$$

where

$$h_k = \begin{pmatrix} \tilde{\epsilon} & \tilde{t} \\ \tilde{t} & \tilde{\epsilon} \end{pmatrix} \quad (\text{B.18})$$

and

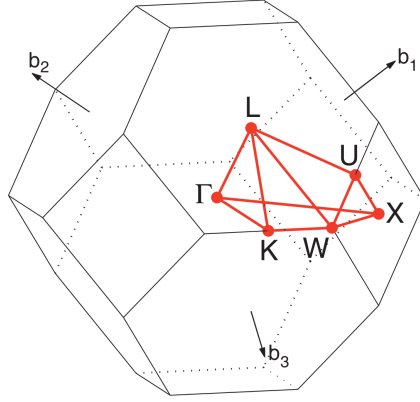


Figure B.3: Brillouin zone of diamond [9]

$$\tilde{t} = t \begin{pmatrix} e^{i\vec{k}\cdot\vec{d}_2} & 0 & 0 & 0 \\ 0 & e^{i\vec{k}\cdot(-\vec{a}_1+\vec{d}_2)} & 0 & 0 \\ 0 & 0 & e^{i\vec{k}\cdot(-\vec{a}_2+\vec{d}_2)} & 0 \\ 0 & 0 & 0 & e^{i\vec{k}\cdot(-\vec{a}_3+\vec{d}_2)} \end{pmatrix} \quad (\text{B.19})$$

The Brillouin zone for the diamond lattice is shown in Fig. B.3. The band structure that results from taking the Γ -L-K- Γ path through the Brillouin zone is shown in Fig. B.4. We compare to an electronic structure calculation for silicon, in Fig. B.5.

It is well known feature of this band structure that it has an indirect bandgap and that silicon is known as an indirect bandgap semiconductor. In the band structure produced with our hopping model for silicon, there is no gap in the Fermi energy. We create a indirect bandgap in that band structure by adding in sub-dominant hopping processes to the model. Fig. B.6 shows such a band structure [72].

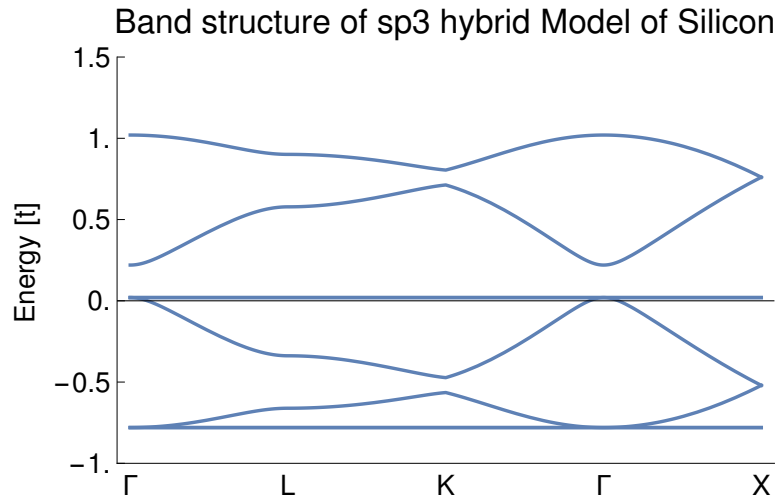


Figure B.4: Band structure of the model $H_{silicon}$ [11]. This band structure results from writing a nearest neighbor hopping model for silicon in the basis of the hybrid orbitals.

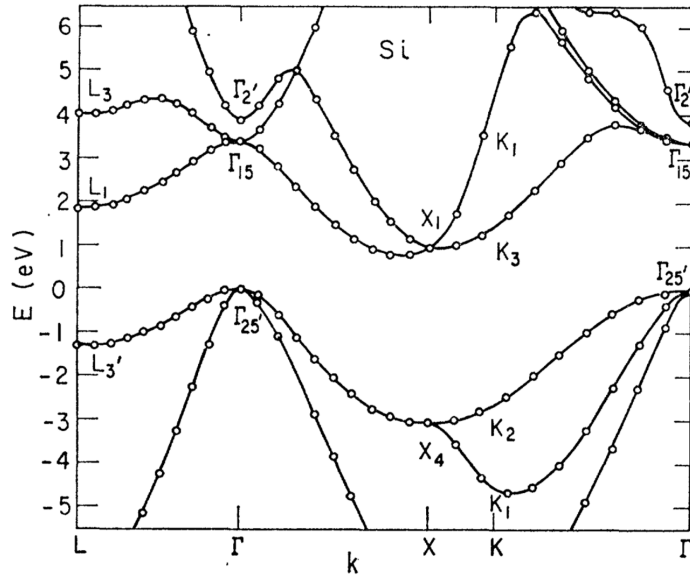


FIG. 1. Band structure of Si.

Figure B.5: Band structure for silicon calculated by pseudopotential method, figure taken with permission from [12]. Looking at this band structure plot, we see that this is an indirect bandgap semiconductor.

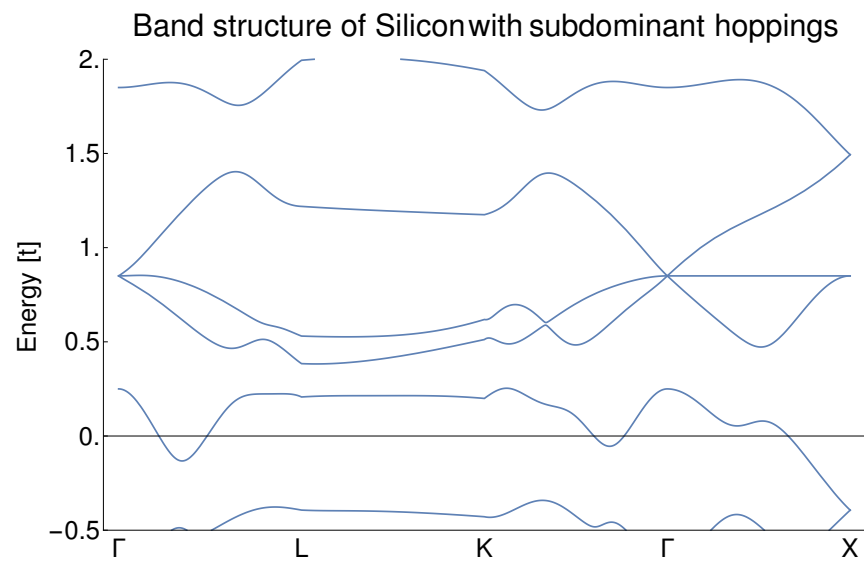


Figure B.6: Band structure for silicon in the hybrid orbital hopping model with sub-dominant hopping terms. Adding in these sub-dominant hopping terms introduces an indirect bandgap, making the band structure found with this model qualitatively like that of the real band structure of silicon.

Appendix C

Dynamic Spin Structure Factor

As we mentioned in the main text, the starting point for our calculation of a dynamic spin structure factor is

$$S(\vec{q}, \omega) = \frac{1}{N_s} \sum_{ij} \int dt \langle \vec{S}_i(0) \cdot \vec{S}_j(t) \rangle e^{-i\vec{q} \cdot (\vec{r}_i - \vec{r}_j)} e^{i\omega t}, \quad (\text{C.1})$$

where \vec{q} is the wavevector measured in neutron scattering, and ω is the energy measured in neutron scattering. We express each of the spins in their Abrikosov Fermion form [69] given by

$$\vec{S}_i = \frac{1}{2} \sum_{\alpha} c_{i\alpha\sigma}^{\dagger} \vec{\tau}_{\sigma\sigma'} c_{i\alpha\sigma'} \quad (\text{C.2})$$

$$= \frac{1}{2} \sum_{\alpha} c_{Rd\alpha\sigma}^{\dagger} \vec{\tau}_{\sigma\sigma'} c_{Rd\alpha\sigma'} \quad (\text{C.3})$$

where here, \vec{R} denotes a Bravais lattice vector, \vec{d} denotes a sublattice vector, α is a d orbital label, and $\vec{\tau}$ is the vector of Pauli matrices.

$$S(\vec{q}, \omega) = \frac{1}{4N_s} \sum_{RdR'd'} \sum_{\alpha\alpha'} \sum_{\sigma\sigma'\sigma''\sigma'''} \int dt \vec{\tau}_{\sigma\sigma'} \cdot \vec{\tau}_{\sigma''\sigma'''}$$
(C.4)

$$\times \langle c_{Rd\alpha\sigma}^\dagger(0) c_{Rd\alpha\sigma'}(0) c_{R'd'\alpha'\sigma''}^\dagger(t) c_{R'd'\alpha'\sigma'''}(t) \rangle e^{-i\vec{q}\cdot((\vec{R}+\vec{d})-(\vec{R}'+\vec{d}'))} e^{i\omega t}$$
(C.5)

Now we express the time-dependent operators as

$$A(t) = e^{\frac{iHt}{\hbar}} A e^{-\frac{iHt}{\hbar}}$$
(C.6)

and we use the completeness relation for the Pauli matrices

$$\vec{\tau}_{\sigma\sigma'} \cdot \vec{\tau}_{\sigma''\sigma'''} = 2\delta_{\sigma\sigma'''}\delta_{\sigma'\sigma''} - \delta_{\sigma\sigma'}\delta_{\sigma''\sigma'''},$$
(C.7)

which gives

$$S(\vec{q}, \omega) = \frac{1}{4N_s} \sum_{RdR'd'} \sum_{\alpha\alpha'} \sum_{\sigma\sigma'\sigma''\sigma'''} \int dt (2\delta_{\sigma\sigma'''}\delta_{\sigma'\sigma''} - \delta_{\sigma\sigma'}\delta_{\sigma''\sigma'''})$$
(C.8)

$$\times \langle c_{Rd\alpha\sigma}^\dagger c_{Rd\alpha\sigma'} e^{-\frac{iHt}{\hbar}} c_{R'd'\alpha'\sigma''}^\dagger c_{R'd'\alpha'\sigma'''} e^{\frac{iHt}{\hbar}} \rangle e^{-i\vec{q}\cdot((\vec{R}+\vec{d})-(\vec{R}'+\vec{d}'))} e^{i\omega t}$$
(C.9)

After this, we Fourier transform using

$$c_{Rd\alpha\sigma} = \frac{1}{\sqrt{N_u}} \sum_k c_{kd\alpha\sigma} e^{i\vec{k}\cdot\vec{R}}$$
(C.10)

which gives

$$S(\vec{q}, \omega) = \frac{1}{4N_s N_u^2} \sum_{RdR'd'} \sum_{\alpha\alpha'} \sum_{\sigma\sigma'\sigma''\sigma'''} \sum_{kk'k''k'''} \int dt (2\delta_{\sigma\sigma'''}\delta_{\sigma'\sigma''} - \delta_{\sigma\sigma'}\delta_{\sigma''\sigma'''}) \quad (\text{C.11})$$

$$\times \langle c_{kd\alpha\sigma}^\dagger c_{k'd\alpha\sigma'} e^{-\frac{iHt}{\hbar}} c_{k''d'\alpha'\sigma''}^\dagger c_{k'''d'\alpha'\sigma'''} e^{\frac{iHt}{\hbar}} \rangle e^{i((-\vec{k}+\vec{k}')\cdot\vec{R}+(-\vec{k}''+\vec{k}''')\cdot\vec{R}')} \quad (\text{C.12})$$

$$\times e^{-i\vec{q}\cdot((\vec{R}+\vec{d})-(\vec{R}'+\vec{d}'))} e^{i\omega t} \quad (\text{C.13})$$

Next we express \vec{R}' in terms of \vec{R} , using $\vec{R}' = \vec{R} + \vec{\eta}$, and we sum over R to get our first condition on the momenta.

$$S(\vec{q}, \omega) = \frac{1}{4N_s N_u^2} \sum_{Rd\eta d'} \sum_{\alpha\alpha'} \sum_{\sigma\sigma'\sigma''\sigma'''} \sum_{kk'k''k'''} \int dt (2\delta_{\sigma\sigma'''}\delta_{\sigma'\sigma''} - \delta_{\sigma\sigma'}\delta_{\sigma''\sigma'''}) \quad (\text{C.14})$$

$$\times \langle c_{kd\alpha\sigma}^\dagger c_{k'd\alpha\sigma'} e^{-\frac{iHt}{\hbar}} c_{k''d'\alpha'\sigma''}^\dagger c_{k'''d'\alpha'\sigma'''} e^{\frac{iHt}{\hbar}} \rangle \quad (\text{C.15})$$

$$\times e^{i((-\vec{k}+\vec{k}'-\vec{k}''+\vec{k}''')\cdot\vec{R})} e^{i(-\vec{k}''+\vec{k}'''+\vec{q})\cdot\vec{\eta}} e^{i\vec{q}\cdot(\vec{d}'-\vec{d})} e^{i\omega t} \quad (\text{C.16})$$

$$= \frac{1}{4N_s N_u} \sum_{d\eta d'} \sum_{\alpha\alpha'} \sum_{\sigma\sigma'\sigma''\sigma'''} \sum_{kk'k''k'''} \int dt (2\delta_{\sigma\sigma'''}\delta_{\sigma'\sigma''} - \delta_{\sigma\sigma'}\delta_{\sigma''\sigma'''}) \quad (\text{C.17})$$

$$\times \langle c_{kd\alpha\sigma}^\dagger c_{k'd\alpha\sigma'} e^{-\frac{iHt}{\hbar}} c_{k''d'\alpha'\sigma''}^\dagger c_{k'''d'\alpha'\sigma'''} e^{\frac{iHt}{\hbar}} \rangle \delta(-\vec{k} + \vec{k}' - \vec{k}'' + \vec{k}''' + \vec{G}) \quad (\text{C.18})$$

$$\times e^{i(-\vec{k}''+\vec{k}'''+\vec{q})\cdot\vec{\eta}} e^{i\vec{q}\cdot(\vec{d}'-\vec{d})} e^{i\omega t} \quad (\text{C.19})$$

To aid us in obtaining this condition on the momenta, we have used the identity

$$\sum_R e^{i\vec{k}\cdot\vec{R}} = N_u \sum_G \delta(\vec{k} + \vec{G}) \quad (\text{C.20})$$

Next we sum over $\vec{\eta}$ and use this identity again to get a second condition on the momenta.

$$S(\vec{q}, \omega) = \frac{1}{4N_s} \sum_{dd'} \sum_{\alpha\alpha'} \sum_{\sigma\sigma'\sigma''\sigma'''} \sum_{kk'k''k'''} \int dt (2\delta_{\sigma\sigma'''}\delta_{\sigma'\sigma''} - \delta_{\sigma\sigma'}\delta_{\sigma''\sigma'''}) \quad (\text{C.21})$$

$$\times \langle c_{kd\alpha\sigma}^\dagger c_{k'd\alpha\sigma'} e^{-\frac{iHt}{\hbar}} c_{k''d'\alpha'\sigma''}^\dagger c_{k'''d'\alpha'\sigma'''} e^{\frac{iHt}{\hbar}} \rangle \quad (\text{C.22})$$

$$\times \delta(-\vec{k} + \vec{k}' - \vec{k}'' + \vec{k}''' + \vec{G}) \delta(-\vec{k}'' + \vec{k}''' + \vec{q} + \vec{G}') e^{i\vec{q}\cdot(\vec{d}'-\vec{d})} e^{i\omega t} \quad (\text{C.23})$$

We then sum over \vec{k}''' , and the delta function sifts and completes the enforcement of the first momentum condition.

$$S(\vec{q}, \omega) = \frac{1}{4N_s} \sum_{dd'} \sum_{\alpha\alpha'} \sum_{\sigma\sigma'\sigma''\sigma'''} \sum_{kk'k''} \sum_G \int dt (2\delta_{\sigma\sigma'''}\delta_{\sigma'\sigma''} - \delta_{\sigma\sigma'}\delta_{\sigma''\sigma'''}) \quad (\text{C.24})$$

$$\times \langle c_{kd\alpha\sigma}^\dagger c_{k'd\alpha\sigma'} e^{-\frac{iHt}{\hbar}} c_{k''d'\alpha'\sigma''}^\dagger c_{(k-k'+k''-G)d'\alpha'\sigma'''} e^{\frac{iHt}{\hbar}} \rangle \quad (\text{C.25})$$

$$\times \delta(\vec{k} - \vec{k}' + \vec{q} + \vec{G}) e^{i\vec{q}\cdot(\vec{d}'-\vec{d})} e^{i\omega t} \quad (\text{C.26})$$

Here we have used the fact that the sum of one reciprocal lattice vector with another is just equal to a reciprocal lattice vector

$$\vec{G}' + \vec{G} \rightarrow \vec{G}' \quad (\text{C.27})$$

We sum over k' now to enforce the second momentum condition

$$S(\vec{q}, \omega) = \frac{1}{4N_s} \sum_{dd'} \sum_{\alpha\alpha'} \sum_{\sigma\sigma'\sigma''\sigma'''} \sum_{kk''} \sum_{GG'} \int dt (2\delta_{\sigma\sigma'''}\delta_{\sigma'\sigma''} - \delta_{\sigma\sigma'}\delta_{\sigma''\sigma'''}) \quad (\text{C.28})$$

$$\times \langle c_{kd\alpha\sigma}^\dagger c_{(k+q+G)d\alpha\sigma'} e^{-\frac{iHt}{\hbar}} c_{k''d'\alpha'\sigma''}^\dagger c_{(k''-q+G')d'\alpha'\sigma'''} e^{\frac{iHt}{\hbar}} \rangle e^{i\vec{q}\cdot(\vec{d}'-\vec{d})} e^{i\omega t} \quad (\text{C.29})$$

After this, we relabel k'' to k' , because there are only 2 remaining momenta. This gives us

$$S(\vec{q}, \omega) = \frac{1}{4N_s} \sum_{dd'} \sum_{\alpha\alpha'} \sum_{\sigma\sigma'\sigma''\sigma'''} \sum_{kk'} \sum_{GG'} \int dt (2\delta_{\sigma\sigma'''} \delta_{\sigma'\sigma''} - \delta_{\sigma\sigma'} \delta_{\sigma''\sigma'''}) \quad (\text{C.30})$$

$$\times \langle c_{kd\alpha\sigma}^\dagger c_{(k+q+G)d\alpha\sigma'} e^{-\frac{iHt}{\hbar}} c_{k'd'\alpha'\sigma''}^\dagger c_{(k'-q+G')d'\alpha'\sigma'''} e^{\frac{iHt}{\hbar}} \rangle e^{i\vec{q}\cdot(\vec{d}'-\vec{d})} e^{i\omega t} \quad (\text{C.31})$$

We insert the resolution of identity,

$$I = \sum_n |n\rangle\langle n|, \quad (\text{C.32})$$

to give

$$S(\vec{q}, \omega) = \frac{1}{4N_s} \sum_{dd'} \sum_{\alpha\alpha'} \sum_{\sigma\sigma'\sigma''\sigma'''} \sum_{kk'} \sum_{GG'} \sum_n \int dt (2\delta_{\sigma\sigma'''} \delta_{\sigma'\sigma''} - \delta_{\sigma\sigma'} \delta_{\sigma''\sigma'''}) \quad (\text{C.33})$$

$$\times \langle Gnd | c_{kd\alpha\sigma}^\dagger c_{(k+q+G)d\alpha\sigma'} | n \rangle \langle n | e^{-\frac{iHt}{\hbar}} c_{k'd'\alpha'\sigma''}^\dagger c_{(k'-q+G')d'\alpha'\sigma'''} e^{\frac{iHt}{\hbar}} | Gnd \rangle \quad (\text{C.34})$$

$$\times e^{i\vec{q}\cdot(\vec{d}'-\vec{d})} e^{i\omega t} \quad (\text{C.35})$$

Since we are looking at inelastic neutron scattering, these states denoted by n are excited states. At this point, we carry out the t integral

$$S(\vec{q}, \omega) = \frac{1}{4N_s} \sum_{dd'} \sum_{\alpha\alpha'} \sum_{\sigma\sigma'\sigma''\sigma'''} \sum_{kk'} \sum_{GG'} \sum_n \int dt (2\delta_{\sigma\sigma'''}\delta_{\sigma'\sigma''} - \delta_{\sigma\sigma'}\delta_{\sigma''\sigma'''}) \quad (\text{C.36})$$

$$\times \langle Gnd | c_{kd\alpha\sigma}^\dagger c_{(k+q+G)d\alpha\sigma'} | n \rangle \langle n | c_{k'd'\alpha'\sigma''}^\dagger c_{(k'-q+G')d'\alpha'\sigma'''} | Gnd \rangle \quad (\text{C.37})$$

$$\times \delta(\omega_{Gnd} - \omega_n + \omega) e^{i\vec{q}\cdot(\vec{d}'-\vec{d})} \quad (\text{C.38})$$

We have used the following result here.

$$\int_{-\infty}^{\infty} dt e^{i\omega t} = 2\pi\delta(\omega) \quad (\text{C.39})$$

After we have inserted the resolution of identity, we express the fermion operators in terms of the matrix elements of the matrix, M, that diagonalizes the Hamiltonian

$$c_{kd\alpha\sigma} = M(k)_{d\alpha\sigma,\lambda} c_{k\lambda} \quad (\text{C.40})$$

and thus we express the structure factor as

$$S(\vec{q}, \omega) = \frac{1}{4N_s} \sum_{dd'} \sum_{\alpha\alpha'} \sum_{\sigma\sigma'\sigma''\sigma'''} \sum_{kk'} \sum_{GG'} \sum_n \sum_{\lambda\lambda'\lambda''\lambda'''} (2\delta_{\sigma\sigma'''}\delta_{\sigma'\sigma''} - \delta_{\sigma\sigma'}\delta_{\sigma''\sigma'''}) \quad (\text{C.41})$$

$$\times \langle Gnd | c_{k\lambda}^\dagger c_{(k+q+G)\lambda'} | n \rangle \langle n | c_{k'\lambda''}^\dagger c_{(k'-q+G')\lambda'''} | Gnd \rangle \quad (\text{C.42})$$

$$\times M(k)_{\lambda,d\alpha\sigma}^\dagger M(k+q+G)_{d\alpha\sigma',\lambda'} M(k')_{\lambda'',d'\alpha'\sigma''}^\dagger M(k'-q+G')_{d'\alpha'\sigma''',\lambda'''} \quad (\text{C.43})$$

$$\times \delta(E_{Gnd} - E_n + \omega) e^{i\vec{q}\cdot(\vec{d}'-\vec{d})} \quad (\text{C.44})$$

The fact that there are two states here, $|n\rangle$ and $|Gnd\rangle$, and that there are operators

connecting them constrains the momentum and eigenstate indices in the following way. There are two cases.

$$k = k + q + G, \quad \lambda = \lambda' \quad (\text{C.45})$$

$$k' = k' - q + G', \quad \lambda'' = \lambda''' \quad (\text{C.46})$$

with $E_\lambda < 0$ and $E_{\lambda''} < 0$

and

$$k = k' - q + G', \quad \lambda = \lambda''' \quad (\text{C.47})$$

$$k' = k + q + G, \quad \lambda' = \lambda'' \quad (\text{C.48})$$

with $E_\lambda < 0$ and $E_{\lambda'} > 0$.

The first case is not of interest to us because we are trying to describe inelastic neutron scattering. Elastic scattering is represented by the first case, and inelastic scattering is represented by the second case. The reason for this is that, in the first case, $E_G = E_n$, which means that there is only a contribution when $\omega = 0$. So, we take a look at the second case. We have also noted here that the case we have chosen is one where $|n\rangle$ is a single-particle excitation state above the ground state, $|Gnd\rangle$ and the energies of these states are related thusly

$$E_{Gnd} - E_n = E_\lambda - E_{\lambda'} \quad (\text{C.49})$$

These energies are related to frequencies. For the purposes of these notes, we set

$\hbar = 1$.

$$\omega_{Gnd} - \omega_n = \frac{E_{Gnd} - E_n}{\hbar} = E_\lambda - E_{\lambda'} \quad (\text{C.50})$$

This leaves us with

$$S(\vec{q}, \omega) = \frac{1}{4N_s} \sum_{dd'} \sum_{\alpha\alpha'} \sum_{\sigma\sigma'\sigma''\sigma'''} \sum_{kk'} \sum_G \sum_{\lambda \in E_\lambda < 0, \lambda' \in E_{\lambda'} > 0} (2\delta_{\sigma\sigma'''}\delta_{\sigma'\sigma''} - \delta_{\sigma\sigma'}\delta_{\sigma''\sigma'''}) \quad (\text{C.51})$$

$$\times M(k)_{\lambda, d\alpha\sigma}^\dagger M(k + q + G)_{d\alpha\sigma', \lambda'} M(k + q + G)_{\lambda', d'\alpha'\sigma''}^\dagger M(k)_{d'\alpha'\sigma''', \lambda} \quad (\text{C.52})$$

$$\times \delta(E_\lambda - E_{\lambda'} + \omega) e^{i\vec{q}\cdot(\vec{d}' - \vec{d})} \quad (\text{C.53})$$

To make the notation more compact, we introduce

$$f(\sigma, \sigma', \sigma'', \sigma''') = M(k)_{\lambda, d\alpha\sigma}^\dagger M(k + q + G)_{d\alpha\sigma', \lambda'} M(k + q + G)_{\lambda', d'\alpha'\sigma''}^\dagger M(k)_{d'\alpha'\sigma''', \lambda} \quad (\text{C.54})$$

Finally, summing over σ'' and σ''' we have

$$S(\vec{q}, \omega) = \frac{1}{4N_s} \sum_{dd'} \sum_{\alpha\alpha'} \sum_{\sigma\sigma'\sigma''\sigma'''} \sum_{kk'} \sum_G \sum_{\lambda \in E_\lambda < 0, \lambda' \in E_{\lambda'} > 0} (2f(\sigma, \sigma', \sigma', \sigma) - f(\sigma, \sigma, \sigma', \sigma')) \quad (\text{C.55})$$

$$\times \delta(E_\lambda - E_{\lambda'} + \omega) e^{i\vec{q}\cdot(\vec{d}' - \vec{d})} \quad (\text{C.56})$$

This is the final result that we see in chapter 4. We use this result to generate a plot that we compare to experiment.

Bibliography

- [1] W. Wu, A. McCollam, I. Swainson, P. M. C. Rourke, D. G. Rancourt, and S. R. Julian. A novel nonFermi-liquid state in the iron-pnictide FeCrAs. *EPL (Europhysics Letters)*, 85(1):17009, jan 2009.
- [2] T. E. Redpath, J. M. Hopkinson, A. A. Leibel, and H.-Y. Kee. Dimensional crossover of a frustrated distorted kagome Heisenberg Model: Application to FeCrAs. *arXiv*, 1:1–8, 2011.
- [3] J. G. Rau and H. Y. Kee. Hidden spin liquid in an antiferromagnet: Applications to FeCrAs. *Physical Review B - Condensed Matter and Materials Physics*, 84(10):104448, 2011.
- [4] S. Ghosh. *Quantum mediated effective interactions for spatially complex systems*. PhD thesis, Cornell, 2015.
- [5] S. Ghosh, P. J. O’Brien, C. L. Henley, and M. J. Lawler. Phase diagram of the Kondo lattice model on the kagome lattice. *Physical Review B*, 93(2):024401, jan 2016.
- [6] P. E. Blochl. Projector augmented-wave method. 50(24):17953–17979, 1994.
- [7] P. J. O’Brien, T. Birol, and M. J. Lawler. Unpublished.
- [8] ElectronicDOS - https://en.wikipedia.org/wiki/Electronic_band_structure.

- [9] W. Setyawan and S. Curtarolo. High-throughput electronic band structure calculations: Challenges and tools. *Computational Materials Science*, 49(2):299–312, 2010.
- [10] Diamond lattice. https://en.wikipedia.org/wiki/Diamond_cubic.
- [11] M. J. Lawler. Condensed Matter Physics Lecture. 2014.
- [12] M. L. Cohen and T. K. Bergstresser. Band structures and pseudopotential form factors for fourteen semiconductors of the diamond and zinc-blende structures. *Physical Review*, 141(2):789–796, 1966.
- [13] G R Stewart. Non-Fermi-liquid behavior in d - and f -electron metals. *Review of Modern Physics*, 73(OCTOBER):797–855, 2001.
- [14] F F Tafti, W Wu, and S R Julian. Non-metallic, non-Fermi-liquid resistivity of FeCrAs from 0 to 17 GPa. *Journal of physics. Condensed matter : an Institute of Physics journal*, 25(38):385601, sep 2013.
- [15] I. P. Swainson, W. Wu, A. McCollam, and S. R. Julian. Non-collinear antiferromagnetism in FeCrAs Special issue on Neutron Scattering in Canada. *Canadian Journal of Physics*, 88(10):701–706, 2010.
- [16] D. G. Rancourt. *Hyperfine Field Fluctuations in the Mossbauer Spectrum of Magnetic Materials: Application to Small Particles and to the Bulk Antiferromagnet Fe(2-x)Cr(x)As*. PhD thesis, University of Toronto, 1984.
- [17] S. Ishida, T. Takiguchi, S. Fujii, and S. Asano. Magnetic properties and electronic structures of CrMZ (M = Fe, Co, Ni; Z = P, As). *Physica B: Condensed Matter*, 217(1-2):87–96, 1996.
- [18] D.-C. He, Y. Peng, and Y.-W. He. Ab Initio Studies on Structural, Elastic,

Thermodynamic and Electronic Properties of FeCrAs under Pressures. *Acta Physica Polonica A*, 127(6):1637–1644, 2015.

- [19] J. M. Florez, P. Vargas, C. Garcia, and C. A. Ross. Magnetic entropy change plateau in a geometrically frustrated layered system: FeCrAs-like iron-pnictide structure as a magnetocaloric prototype. *Journal of physics. Condensed matter : an Institute of Physics journal*, 25(22):226004, 2013.
- [20] A. Akrap, Y. M. Dai, W. Wu, S. R. Julian, and C. C. Homes. Optical properties and electronic structure of the nonmetallic metal FeCrAs. *Physical Review B - Condensed Matter and Materials Physics*, 89(12):125115, 2014.
- [21] S L Dudarev, G A Botton, S Y Savrasov, C J Humphreys, and A P Sutton. Electron-energy-loss spectra and the structural stability of nickel oxide:. 57(3):1505–1509, 1998.
- [22] A. I. Liechtenstein, V. I. Anisimov, and J. Zaanen. strong interactions: Orbital ordering. *Physical Review B*, 52(8):5467–5471, 1995.
- [23] D. C. Langreth and J. P. Perdew. Theory of nonuniform electronic systems. I. Analysis of the gradient approximation and a generalization that works. 21(12), 1980.
- [24] I. Martin and C. D. Batista. Itinerant electron-driven chiral magnetic ordering and spontaneous quantum hall effect in triangular lattice models. *Physical Review Letters*, 101(15):156402, 2008.
- [25] Y. Akagi and Y. Motome. Spin Chirality Ordering and Anomalous Hall Effect in the Ferromagnetic Kondo Lattice Model on a Triangular Lattice. *Journal of the Physical Society of Japan*, 79(8):4, 2010.

- [26] L. Messio, B. Bernu, and C. Lhuillier. Kagome antiferromagnet: A chiral topological spin liquid? *Physical Review Letters*, 108(20):207204, 2012.
- [27] Y. Akagi, M. Udagawa, and Y. Motome. Hidden multiple-spin interactions as an origin of spin scalar chiral order in frustrated Kondo lattice models. *Physical Review Letters*, 108(9):096401, 2012.
- [28] G.-W. Chern. Noncoplanar magnetic ordering driven by itinerant electrons on the pyrochlore lattice. *Physical Review Letters*, 105(22):226403, 2010.
- [29] G.-W. Chern. Novel Magnetic Orders and Ice Phases in Frustrated Kondo-Lattice Models. *Spin*, 05(02):1540006, 2015.
- [30] R.J. Cava, A.P. Ramirez, Q. Huang, and J.J. Krajewski. Compounds with the YbFe₂O₄Structure Type: Frustrated Magnetism and Spin-Glass Behavior. *Journal of Solid State Chemistry*, 140(2):337–344, 1998.
- [31] D. Grohol, K. Matan, J.-H. Cho, S.-H. Lee, J. W. Lynn, Daniel G Nocera, and Young S Lee. Spin chirality on a two-dimensional frustrated lattice. *Nature materials*, 4(4):323–328, 2005.
- [32] Y. Huang, K. Chen, Y. Deng, N. Prokof’Ev, and B. Svistunov. Spin-Ice State of the Quantum Heisenberg Antiferromagnet on the Pyrochlore Lattice. *Physical Review Letters*, 116(17):24–26, 2016.
- [33] M. J. Lawler, H. Y. Kee, Y. B. Kim, and A. Vishwanath. Topological spin liquid on the hyperkagome lattice of Na₄Ir₃O₈. *Physical Review Letters*, 100(22):4–7, 2008.
- [34] M. J. Lawler. Emergent gauge dynamics of highly frustrated magnets. *New Journal of Physics*, 15, 2013.

- [35] S.-H. Lee, C. Broholm, M. F. Collins, L. Heller, A. P. Ramirez, Ch. Kloc, E. Bucher, R. W. Erwin, and N. Lacevic. Less than 50% sublattice polarization in an insulating $S=3/2$ kagomé antiferromagnet at $T \approx 0$. *Physical Review B*, 56(13):8091–8097, 1997.
- [36] S.-H. Lee, C. Broholm, T. H. Kim, W. Ratcliff, and S-W. Cheong. Local Spin Resonance and Spin-Peierls-like Phase Transition in a Geometrically Frustrated Antiferromagnet. *Physical Review Letters*, 84(16):3718–3721, 2000.
- [37] S.-H. Lee, H. Takagi, D. Louca, M. Matsuda, S. Ji, Hiroaki Ueda, Yutaka Ueda, Takuro Katsufuji, Jae Ho Chung, Sungil Park, Sang Wook Cheong, and Collin Broholm. Frustrated magnetism and cooperative phase transitions in spinels. *Journal of the Physical Society of Japan*, 79(1):1–14, 2010.
- [38] L. Messio, C. Lhuillier, and G. Misguich. Lattice symmetries and regular magnetic orders in classical frustrated antiferromagnets. *Physical Review B - Condensed Matter and Materials Physics*, 83(18):184401, 2011.
- [39] R. Moessner and J. T. Chalker. Properties of a classical spin liquid: the Heisenberg pyrochlore antiferromagnet. *Physical Review Letters*, 80(13):2929, 1998.
- [40] R. Moessner and J. T. Chalker. Low-temperature properties of classical geometrically frustrated antiferromagnets. *Physical Review B*, 58(18):12049–12062, 1998.
- [41] R. Moessner and A. P. Ramirez. Geometrical frustration. *Physics Today*, 59(2):24–29, 2006.
- [42] S. Nakatsuji, Y. Machida, Y. Maeno, T. Tayama, T. Sakakibara, J. Van Duijn, L. Balicas, J. N. Millican, R. T. MacAluso, and J. Y. Chan. Metallic spin-liquid behavior of the geometrically frustrated kondo lattice $\text{Pr}_2\text{Ir}_2\text{O}_7$. *Physical Review Letters*, 96(8):3–6, 2006.

- [43] B. Normand. Frontiers in frustrated magnetism. *Contemporary Physics*, 50(4):533–552, 2009.
- [44] A. P. Ramirez. Strongly Geometrically Frustrated Magnets. *Annual Review of Materials Science*, 24:453–480, 1994.
- [45] S. R. Sklan and C. L. Henley. Nonplanar ground states of frustrated antiferromagnets on an octahedral lattice. *Physical Review B - Condensed Matter and Materials Physics*, 88(2):024407, 2013.
- [46] E. S. Sørensen, M. J. Lawler, and Y. B. Kim. Néel and valence-bond crystal order on a distorted kagome lattice: Implications for Zn-paratacamite. *Physical Review B - Condensed Matter and Materials Physics*, 79(17):4–9, 2009.
- [47] J. Sugiyama, H. Nozaki, J. H. Brewer, E. J. Ansaldo, G. D. Morris, and C. Delmas. Frustrated magnetism in the two-dimensional triangular lattice of $\text{Li}_{\text{x}}\text{CoO}_2$. *Physical Review B*, 72(14):144424, 2005.
- [48] L. Balents. Spin liquids in frustrated magnets. *Nature*, 464(7286):199–208, 2010.
- [49] S. Doniach. The Kondo lattice and weak antiferromagnetism. *Physica B+C*, 91(C):231–234, 1977.
- [50] A. P. Ramirez, A. Hayashi, R. J. Cava, R. Siddharthan, and B. S. Shastry. Zero-point entropy in /‘spin ice’/. *Nature*, 399(110):333–335, 1999.
- [51] S. T. Bramwell and M. J. P. Gingras. Spin Ice State in Frustrated Magnetic Pyrochlore Materials. *Science*, 294(5546):1495–1501, 2001.
- [52] Y. Kato, I. Martin, and C. D. Batista. Stability of the spontaneous quantum hall state in the triangular Kondo-lattice model. *Physical Review Letters*, 105(26):1–4, 2010.

- [53] Y. Akagi and Y. Motome. Ground-state Phase Diagram of the Kondo Lattice Model on Triangular-to-kagome Lattices. *J. Korean Phys. Soc.*, 63:405, 2013.
- [54] K. Barros, J. W. F. Venderbos, G.-W. Chern, and C. D. Batista. Exotic magnetic orderings in the kagome Kondo-lattice model. *Physical Review B - Condensed Matter and Materials Physics*, 90(24):1–13, 2014.
- [55] B. O. Sung and M. J. Lawler. Order by disorder decision making via Berry flux. *Physical Review B*, 94(14):144438, 2016.
- [56] M. Foss-Feig, M. Hermele, and A.-M. Rey. Probing the kondo lattice model with alkaline-earth-metal atoms. *Physical Review A - Atomic, Molecular, and Optical Physics*, 81(5):3–6, 2010.
- [57] J. Silva-Valencia and A. M. C. Souza. Entanglement of alkaline-earth-metal fermionic atoms confined in optical lattices. *Physical Review A - Atomic, Molecular, and Optical Physics*, 85(3):4–7, 2012.
- [58] J. H. Van Vleck. Theory of the variations in paramagnetic anisotropy among different salts of the iron group. *Physical Review*, 41(2):208–215, 1932.
- [59] M. A. Ruderman and C. Kittel. Indirect exchange coupling of nuclear magnetic moments by conduction electrons. *Physical Review*, 96(1):99–102, 1954.
- [60] T. Kasuya. A Theory of Metallic Ferro- and Antiferromagnetism on Zener’s Model. *Progress of Theoretical Physics*, 16(1):45–57, 1956.
- [61] K. Yosida. Magnetic properties of Cu-Mn alloys. *Physical Review*, 106(5):893–898, 1957.
- [62] C. Zener. Interaction between the d-shells in the transition metals. II. Ferromagnetic compounds of manganese with Perovskite structure. *Physical Review*, 82(3):403–405, 1951.

- [63] P. W. Anderson and H. Hasegawa. Considerations on double exchange. *Physical Review*, 100(2):675–681, 1955.
- [64] P. G. De Gennes. Effects of double exchange in magnetic crystals. *Physical Review*, 118(1):141–154, 1960.
- [65] M. P. Marder. *Condensed Matter Physics*. 2010.
- [66] K. Varga and J. A. Driscoll. *Computational Nanoscience: Applications for Molecules, Clusters, and Solids*. 2011.
- [67] M. F. Lapa and C. L. Henley. Ground States of the Classical Antiferromagnet on the Pyrochlore Lattice. *Arxiv*, page 19, 2012.
- [68] V. J. Emery. Theory of high-T_c superconductivity in oxides. *Physical Review Letters*, 58(26):2794–2797, 1987.
- [69] Y.-M. Lu, G.-Y. Cho, and A. Vishwanath. Unification of bosonic and fermionic theories of spin liquids on the kagome lattice. *arXiv*, 19:4, 2014.
- [70] A. Altland and B. D. Simons. *Condensed Matter Field Theory*. Cambridge University Press, 2010.
- [71] P. Hofmann. *Solid State Physics*. 2008.
- [72] K. Sherman. Indirect Bandgap Semiconductor. *Michael Lawler's Condensed Matter Physics class*, 2014.